



J, J. A., Schneider, J., Ubaid, J., Velmurugan, R., Gupta, N.K. and Kumar, S. (2021) Energy absorption characteristics of additively manufactured plate-lattices under low- velocity impact loading. *International Journal of Impact Engineering*, 149, 103768. (doi: [10.1016/j.ijimpeng.2020.103768](https://doi.org/10.1016/j.ijimpeng.2020.103768))

The material cannot be used for any other purpose without further permission of the publisher and is for private use only.

There may be differences between this version and the published version. You are advised to consult the publisher's version if you wish to cite from it.

<http://eprints.gla.ac.uk/226035/>

Deposited on 09 November 2020

Enlighten – Research publications by members of the University of
Glasgow

<http://eprints.gla.ac.uk>

1 Energy absorption characteristics of additively manufactured plate-lattices under low-
2 velocity impact loading

3
4 Jefferson Andrew J^a, Johannes Schneider^{a,b}, Jabir Ubaid^a, R Velmurugan^c, N K Gupta^d, S Kumar^{a,b,*}

5 ^aDepartment of Mechanical Engineering, Khalifa University of Science and Technology, Masdar Campus, Masdar
6 City, P.O. Box 54224, Abu Dhabi, UAE.

7 ^bJames Watt School of Engineering, University of Glasgow, Glasgow G12 8LT, UK.

8 ^cDepartment of Aerospace Engineering, Indian Institute of Technology Madras, Chennai 600036, India

9 ^dDepartment of Applied Mechanics, Indian Institute of Technology Delhi, New Delhi 110016, India.

10 *Corresponding author: s.kumar@eng.oxon.org

11 **Abstract**

12 This study is focused on the low-velocity impact response of 3D plate-lattices fabricated via
13 stereolithography additive manufacturing (AM). Elementary (SC, BCC and FCC) and hybrid (SC-BCC,
14 SC-FCC and SC-BCC-FCC) configurations were tested and the effects of impact energy, relative density,
15 plate-thickness, multiple impacts and impact angle on the dynamic crushing behavior and energy absorption
16 characteristics were analyzed. The experimental results reveal that the hybrid lattices, due to the existence
17 of larger number of open and closed sub-cells, were able to attenuate the peak impact stress transmitted to
18 the structure and extend the duration of the load pulse (high toughness). A significant energy dependency
19 of contact force-displacement characteristics of hybrid structures was noticed with increase in impact
20 energy. The SC-BCC-FCC hybrid plate-lattices depicted a 70% increase in toughness and their specific
21 energy absorption capacity is higher than the conventional aluminum lattices and other practical
22 metamaterials. Experimental observations also revealed that the distribution of plates in each elementary
23 structure in hybrid configuration plays an important role in mitigating the deleterious failure mode by
24 transforming the brittle mode fracture into progressive damage of the plate-lattices. This paper, believed to
25 be the first comprehensive experimental study, discusses the role of relative density, plate-thickness,
26 multiple impacts, impact energy and oblique impact on the low velocity impact response of geometrically
27 hybridized plate-lattice structures. The results of this investigation suggest that the concept of hybridization
28 of plate-lattice architectures in conjunction with AM will enable development of lightweight high impact
29 energy absorbing structures for a wide variety of applications.

30 **Keywords:** Low-velocity impact, plate-lattice structures, energy absorption, impact resistance, oblique
31 impact, cellular structures

32 1. Introduction

33 Lightweight cellular structures have been extensively used for aerospace, thermal, biomedical and
34 transportation applications due to their extraordinary properties such as high specific strength, superior
35 vibration attenuation, low thermal conductivity and excellent energy absorption characteristics [1, 2].
36 Cellular structures are produced by appropriately combining solid material and void space to reduce the
37 effective density [3] and are therefore extensively used for energy absorbing protective devices and packing
38 [4]. These structures can endure a large compressive strain at almost a constant stress, absorbing a large
39 amount of energy devoid of transferring a high stress to the protected object [5, 6].

40 Based on the configuration of pores, cellular structures can be grouped two broad categories:
41 periodic porous structures and random stochastic foams [7]. Usually, the former (periodic porous structures)
42 contain regular and repeating unit-cells whose mechanical properties can be easily tailored. Random
43 stochastic foams are the first generation of manmade porous-isotropic materials extensively employed for
44 impact energy absorption applications and elastic cushioning [8]. The random assembly of closed and open
45 cells in stochastic foams enables them to achieve the direction-independent stress-strain response.
46 Compared to random stochastic foams, periodic lattice structures have considerably higher mechanical
47 properties. This is owing to the reason that, under a mechanical stress (static or dynamic loading), periodic
48 lattice structures have unit-cell elements that predominantly stretch and/or compress while stochastic foams
49 with random microstructures predominantly bend [9]. As the configuration of these materials at the micron
50 scale plays a vital role on their macroscopic performance and mechanical properties [3, 10], researchers
51 have developed better replacements for foam structures.

52 Lattice structures can overcome the aforementioned limitations of foams to a great extent. In terms
53 of strength and stiffness, truss-lattice structures surpass stochastic foams for the same relative density and
54 basis material [8, 11]. Lattice structures are extremely efficient but not easily producible by conventional
55 methods. Emerging advances in additive manufacturing (AM) has enabled the fabrication of lattice
56 structures over a range of length scales [12-14]. One of the main advantages of AM is geometric freedom
57 as it enables the fabrication of complex near net-shape configuration directly from the CAD models,
58 addressing the necessity for highly customized components with improved functionality [15-17]. [18] [17,
59 19, 20].

60 Extant computational and experimental investigations led to a better understanding of the
61 mechanical response of 3D truss-lattices [12, 21]. Mechanical properties of truss-lattice structures under
62 quasi-static and dynamic loading conditions have been widely investigated [22-24]. The design of lattice
63 structure involves the choice of (a) the manufacturing technology, (b) the material system, (c) the geometry
64 and (d) the relative density with respect to bulk specimens [23] [25] [26] [27] [28] [29] [30] [31] [32].

65 Regardless of their dominance in stiffness to random foams, the structural performance of the
66 stiffest truss-lattices is still not the best. For instance, at a low relative density, their stiffness is below 33%
67 of the Hashin-Shtrikman bound (the maximum theoretically attainable elastic modulus for an isotropic
68 porous solid) [33, 34]. Recently, a new group of lattice structures rereferred to as plate-lattices is attracting
69 interest among researchers due to their potential applications in lightweight-energy absorption components
70 [12]. Berger et al. [35], using numerical analysis, reported that plate-lattice structures were capable of
71 achieving a maximum theoretical stiffness. Plate-lattices are up to three times stiffer than optimal trusses
72 of equal mass. Lattice structures made of shells and plates seem to be more promising [36]. Hybrid lattice-
73 structures (i.e. combination of elementary structures: namely, simple cubic (SC), body centered cubic
74 (BCC) and face centered cubic (FCC)) can generate combinations of mechanical properties that are
75 different from the constituent properties and are extremely reliant on both, the comparative proportion of
76 solid material and void space (relative density) along with the structural topology (unit cell architecture).
77 This combination produces an engineered metamaterial capable of providing effective mechanical
78 properties not found in nature. Recently, Thomas et al. [12] investigated the quasi-static compressive
79 behavior of different elementary and combined lattice structures made of photo-resins fabricated by photon
80 polymerization direct laser writing technique. In their investigation, the compressive responses of plate-
81 lattice and truss-lattice structures with various relative densities were studied. Their study revealed that the
82 combination of various elementary plate-lattices at an optimum proportion improved both, the yield
83 strength and stiffness properties. Their study also demonstrated the role of each elementary structure in
84 supporting the whole combined structure to achieve the directional-independent performance
85 enhancements.

86 The aforementioned studies have largely focused on the quasi-static compression response of 3D
87 plate-lattice structures [12, 35, 36]. To date, no experimental evidence on the dynamic impact behavior of
88 plate-lattice structures has been reported. The study of low-velocity impact response of plate-lattice
89 structures is indispensable as such structures quite frequently experience transient impact loads in practice.
90 Although plate-lattices come under cellular materials, certain concepts differ from the well-studied truss-
91 lattice structures, mainly under transient impact loading conditions [37]. The mechanical behavior of 3D
92 plate-lattice structures may depict quite distinctive differences under quasi-static and transient impact loads,
93 due to their rate-sensitivity [38]. In cellular structures, the mechanisms of rate-sensitivity include the micro-
94 inertia effects, the material's strain-rate dependency, the compression and movement of air stuck in cells,
95 the shock wave effects and the geometrical effects [37, 39]. Numerous experimental and numerical
96 investigations have been performed on cellular structures to highlight the mechanisms inducing rate-
97 sensitivity [37-39]. The huge potential of using lattice-structures in light-weight high performance
98 applications [12, 35] necessitates the investigation on low velocity impact response of plate-lattices.

99 Numerous authors have investigated the response of cellular structures under transverse impacts
100 [7, 40, 41]. However, normal impacts do not often occur in practice and structures are more often impacted
101 at some oblique angles [42]. Moreover, depending on the impact angle of the striker with respect to the
102 target, impact response and damage mechanisms may vary [43]. In the case of architected materials such
103 as truss-lattices, honeycombs and plate-lattices, it is less apparent to know the impact direction sensitivity
104 of their impact response. For instance, a simple-cubic plate-lattice unit cell with three orthogonal plates
105 exhibits the same response along the transverse and longitudinal directions, however, it is very anisotropic:
106 its response along the diagonal directions is a few orders of magnitude lower [44]. At microstructural scale,
107 anisotropy can be leveraged to obtain high strength in conjunction with high damage tolerance [45].
108 Nevertheless, at the macroscopic scale, engineered metamaterials for large volume applications are
109 expected to reveal isotropic properties [46]. In cellular structures, the impact response often relies on the
110 orientation of different structural members and distribution of materials with respect to the direction of
111 impact [47]. To date, no investigation has concentrated on the oblique impact behavior of plate-lattices.

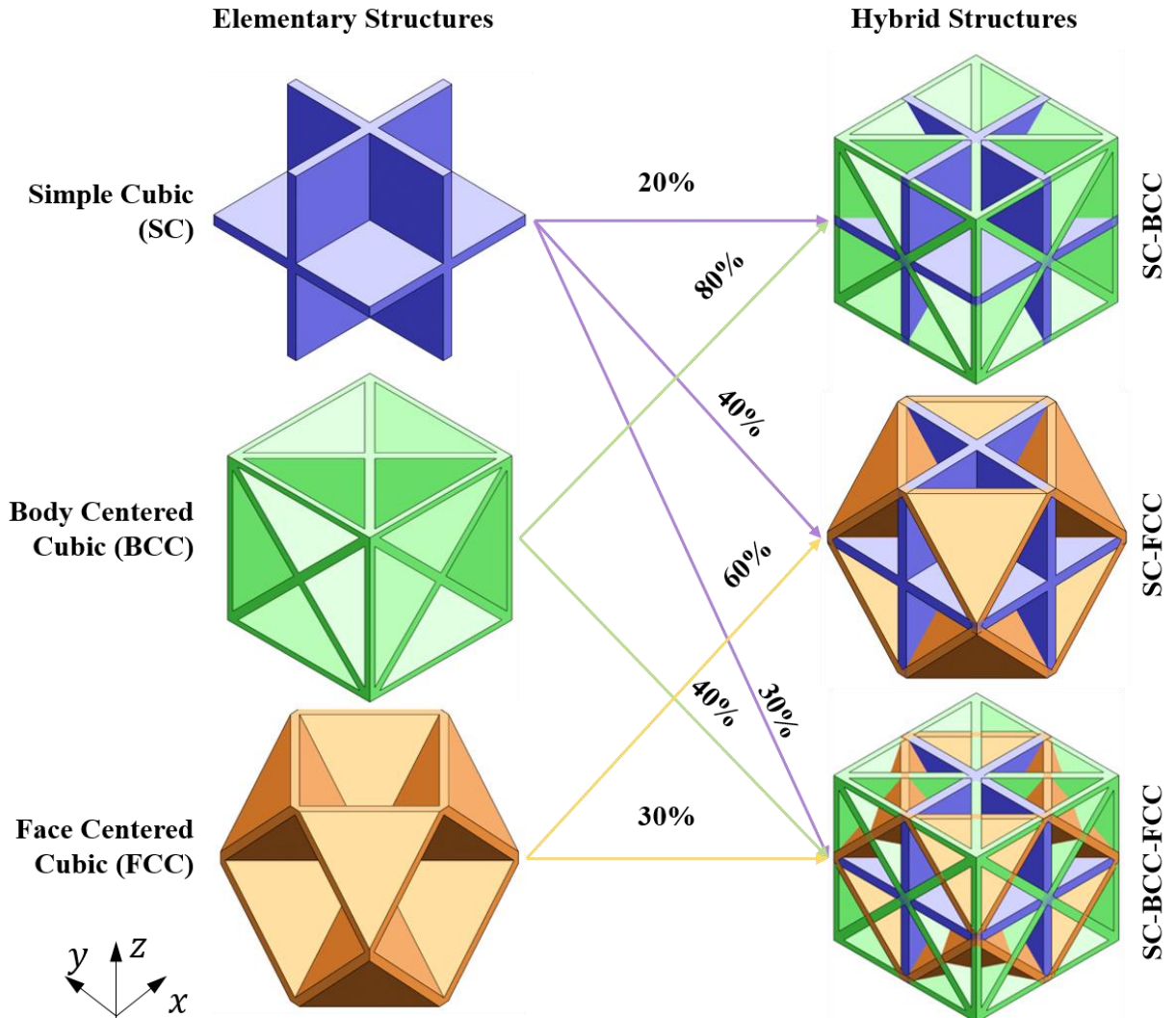
112 Motivated by the present knowledge gap in the impact performance of 3D plate-lattice structures
113 and the paucity of experimental information, this paper aims at examining the dynamic crushing behavior
114 and energy absorption characteristics of 3D plate-lattice structures under low velocity impact loading
115 experimentally. To the best of authors' knowledge, this study is the first to experimentally investigate the
116 impact response of cellular structures at various angles of impact, despite the fact that cellular structures
117 have been used for decades as light-weight energy absorbing structures. The 3D plate-lattice structures are
118 fabricated from polymeric material (PlasGRAYTM) using stereolithography-based 3D-printing technique.
119 The lattice specimens were subjected to low-velocity impacts using a drop tower setup to analyze their
120 energy absorption properties and damage mechanisms. The measurements were used to examine effects of
121 relative density, wall thickness, impact angle, impact energy and multiple impacts on the impact
122 performance of AM-enabled 3D plate-lattice structures.

123 **2. Experimental Procedure**

124 **2.1 Specimen fabrication through 3D printing**

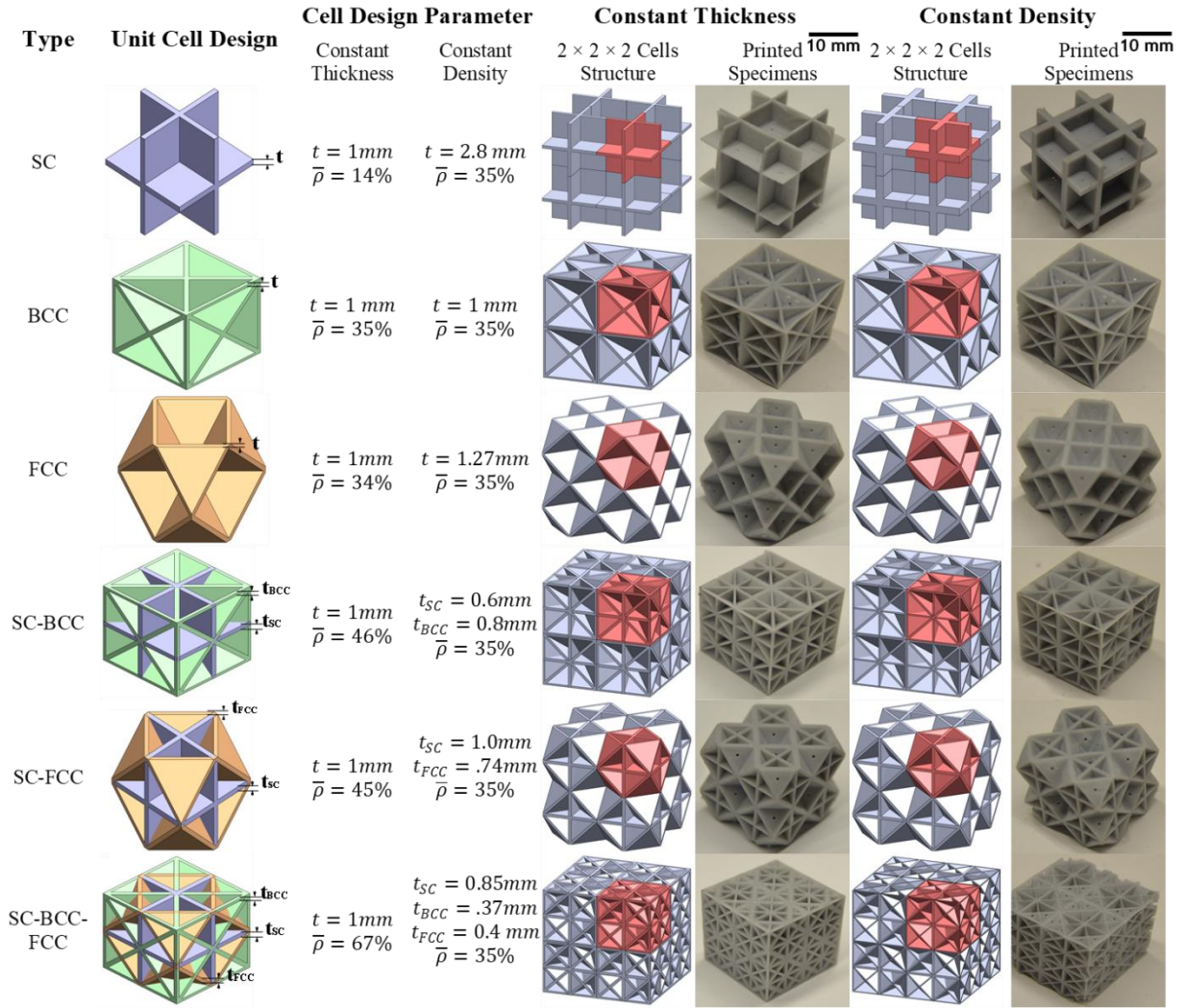
125 Dynamic behavior of 3D plate-lattice structures are strongly influenced by the core structure [12].
126 In this study, six types of core topologies were analyzed: three elementary structures namely, simple cubic
127 (SC), body centered cubic (BCC) and face centered cubic (FCC) and three hybrid structures viz., SC-BCC,
128 SC-FCC and SC-BCC-FCC. The main objective is to investigate the individual and associated effects of
129 the relative density, thickness distribution and topology on the energy absorption characteristics and
130 damage behavior of plate-lattice structures. Therefore, plate-lattice specimens with constant relative density
131 and constant plate-thickness were fabricated separately. For the former case, the relative density ($\bar{\rho}$) was

132 set to be 35% against the bulk material. Hence, the thickness of the plates in different architectures varied
 133 depending upon the volume of the plates in each lattice. In the hybrid specimens, the different elementary
 134 structures were combined as per the optimal volumetric proportion suggested in [12], so that their behavior
 135 is directional-independent in the linear elastic regime (see [Figure 1](#)Figure-1).



136
 137 *Figure 1: Schematic depicting the proportion of elementary structures in the hybrid plate-lattice structures.*

138 In the constant thickness case, the thickness of all the plates in the lattice structures were kept equal
 139 (i.e. 1 mm), while varying the relative density. This further allows to study how the distribution of plate-
 140 lattice thickness influences the impact response of various plate-lattice configurations. All the plate-lattice
 141 specimens were fixed to have the same dimension of the unit cell, i.e., 16 mm. The specimens tested
 142 consisted of eight unit cells ($2 \times 2 \times 2$). The unit cell design and cell design parameters of various plate-
 143 lattice specimens are depicted in [Figure 2](#)Figure-2.



144

145 *Figure 2: The unit cell design, cell design parameters, CAD models and printed specimens of various plate-*
 146 *lattice structures.*

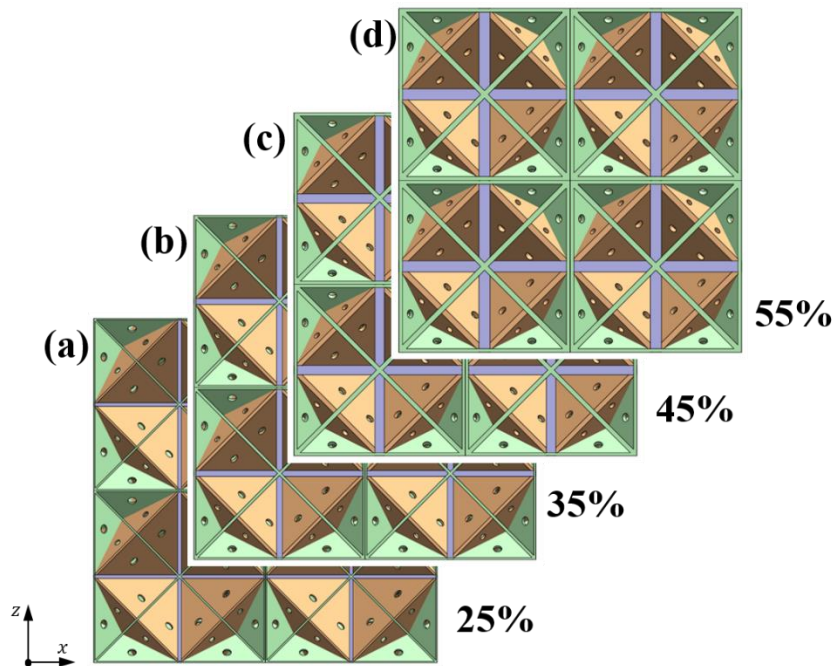
147 *Table 1: Specimen code and wall thickness of SC-BCC-FCC specimens for different relative densities*

Specimen code	Relative Density (%)	Wall Thickness (mm)		
		SC	BCC	FCC
R25	25	0.42	0.2	0.18
R35	35	0.7	0.32	0.3
R45	45	1.1	0.52	0.45
R55	55	1.3	0.62	0.55

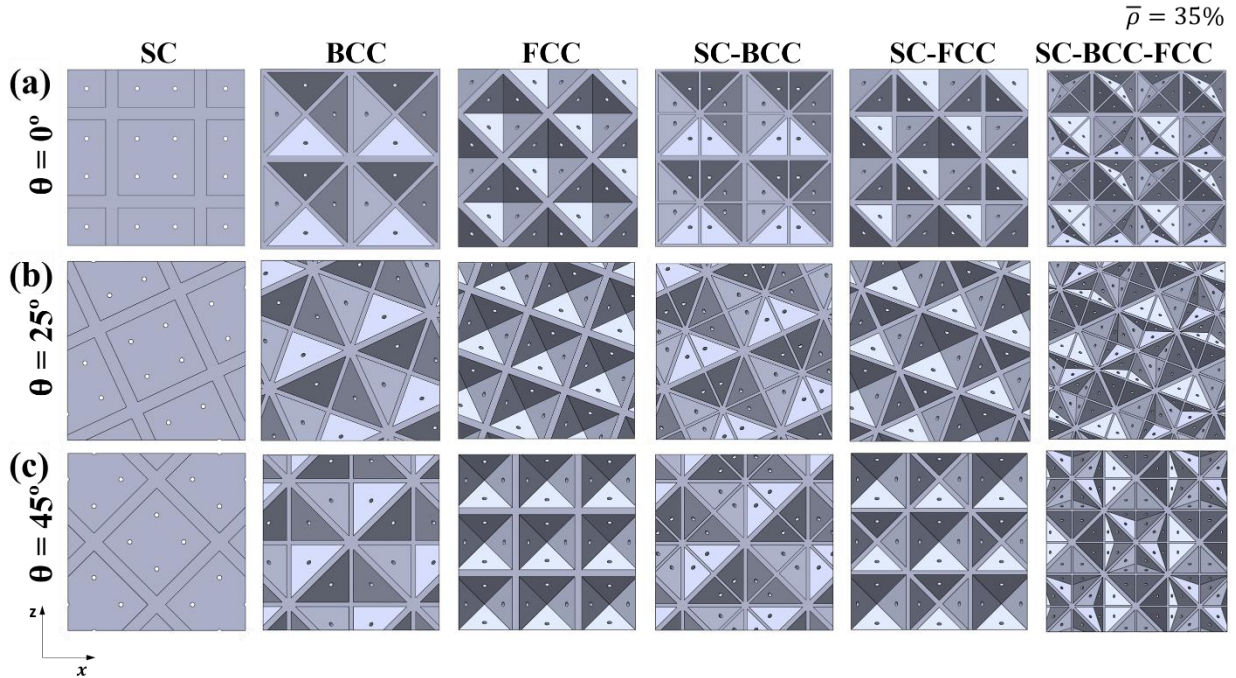
148

167 To specifically study the role of relative density, SC-BCC-FCC specimens with four different
 168 relative densities (25%, 35%, 45% and 55%) were fabricated and the volume fraction of their elementary
 169 constituents SC, BCC and FCC were set to 30%, 40% and 30%, respectively. *Figure 3* depicts the
 170 CAD models of SC-BCC-FCC specimens with various relative densities. *Table 1*: summarizes the
 171 specimen code and wall thickness of elementary structures in various SC-BCC-FCC specimens. To
 172 examine the effect of oblique impact and to study the complete flat-wise dynamic compression behavior of
 173 various plate-lattice specimens, the unit cells of various specimens were rotated at 0° , 25° and 45° with
 174 respect to the face of the impactor, as illustrated in *Figure 4*, while the overall dimensions were
 175 scaled down from aforementioned unit cell size of 16 mm and kept fixed at $20 \times 20 \times 20$ mm.

176 All the 3D plate-lattice specimens were fabricated using slide and separate™ (SAS™) 3D printing
 177 employing a PRO2-ASIGA desktop 3D printer. SAS™ enables a large build area while inducing the lowest
 178 fabrication forces of any upside-down stereolithography (SLA) technology (layer by layer) enabled system.
 179 The process parameters employed for fabricating the plate-lattice specimens are summarized in Table S1.
 180 The plate-lattice specimens were printed employing PlasGRAY™ thermoplastic material whose properties
 181 are summarized in *Table S2*.



182 *Figure 3*: Geometries of SC-BCC-FCC specimens with various relative densities (a) 25%, (b) 35%, (c) 45%
 183 and (d) 55%.



185
186 Figure 4: Different plate-lattice specimens rotated in counter clockwise direction at (a) 0° , (b) 25° and (c)
187 45° with respect to the face of the impactor (constant relative density, $\bar{\rho} = 35\%$).

188 2.2 Low-velocity impact tests

189 Dynamic low velocity impact tests were performed using a CEAST 9350 drop weight impact tower
190 to evaluate the energy absorption characteristics of the plate-lattice specimens. The impact setup consists
191 of a dynamic load cell, a laser displacement transducer, a braking system and a data acquisition system.
192 During the test, the resistive contact force experienced by the specimens on the impactor was measured by
193 a piezoelectric dynamic load cell of maximum load capacity 30 kN. An instrumented cylindrical flat-face
194 impactor with a diameter of 60 mm and a mass of 16.748 kg was employed to impact onto the flat top-side
195 of the specimens. Before testing, the lattice specimens were aligned and placed with respect to the impactor.
196 The lattice specimens were placed on a rigid base to examine the pure dynamic compression behavior under
197 impact load. With such support or boundary conditions, no impact energy can be dissipated through global
198 bending of the lattice specimens. Specimens have been impacted at different impact energy levels by
199 maintaining a constant impactor mass (16.748 kg). [Table 2](#) summarizes the impact heights chosen
200 in this investigation, as well as the corresponding impact velocities and energies.

201 A laser device measured the velocity history of the impactor before and after the impact event. A
202 four channel CEAST DAS 64k high speed data acquisition unit was employed to sample the signals picked
203 up by the load cell and the laser gate. The signal sampling frequency of the data acquisition system was set
204 to 3 MSPS (Million Samples per Second). After performing the first impact test on the specimen, a brake

205 mechanism was triggered to avoid a second strike. From the basic contact force–displacement and energy-
206 time curves, important parameters such as peak force, absorbed energy, contact duration and maximum
207 displacement were calculated. At least five impact tests were repeated for each specimen category.

208 *Table 2: Summary of impact height, velocity and energy used in the tests*

Impact Height (mm)	Impact Velocity (m/s)	Impact Energy (J)
91	1.54	20
209	2.18	40
315	2.67	60
457	3.09	80

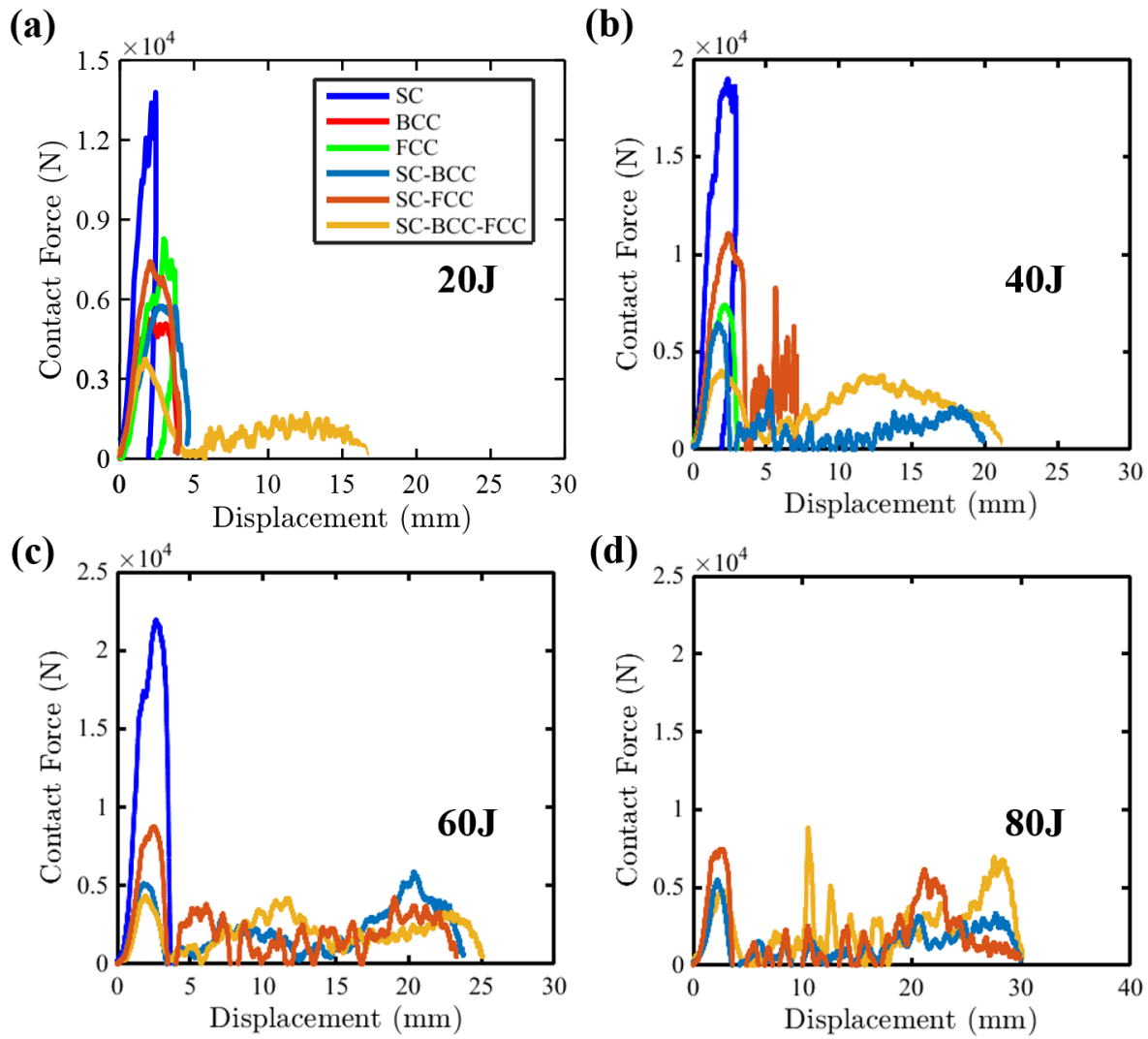
209
210 Two types of test protocols were used, namely, (i) single impact test protocol, where the specimens
211 were subjected to a single impact event up to complete crushing threshold (20-80 J), and (ii) multiple impact
212 test protocol where six repetitive impacts were performed on the same specimens at lower impact energy
213 levels between 20-60 J. For repeated impact tests, the low impact energy levels of 20, 40 and 60 J were
214 preferred with the aim of being adequately far from the complete crushing threshold of hybrid plate-lattice
215 specimens (80 J) in order to examine their capability of sustaining repeated impacts in the presence of
216 moderate amount of impact damage.

217 **3. Results and discussion**

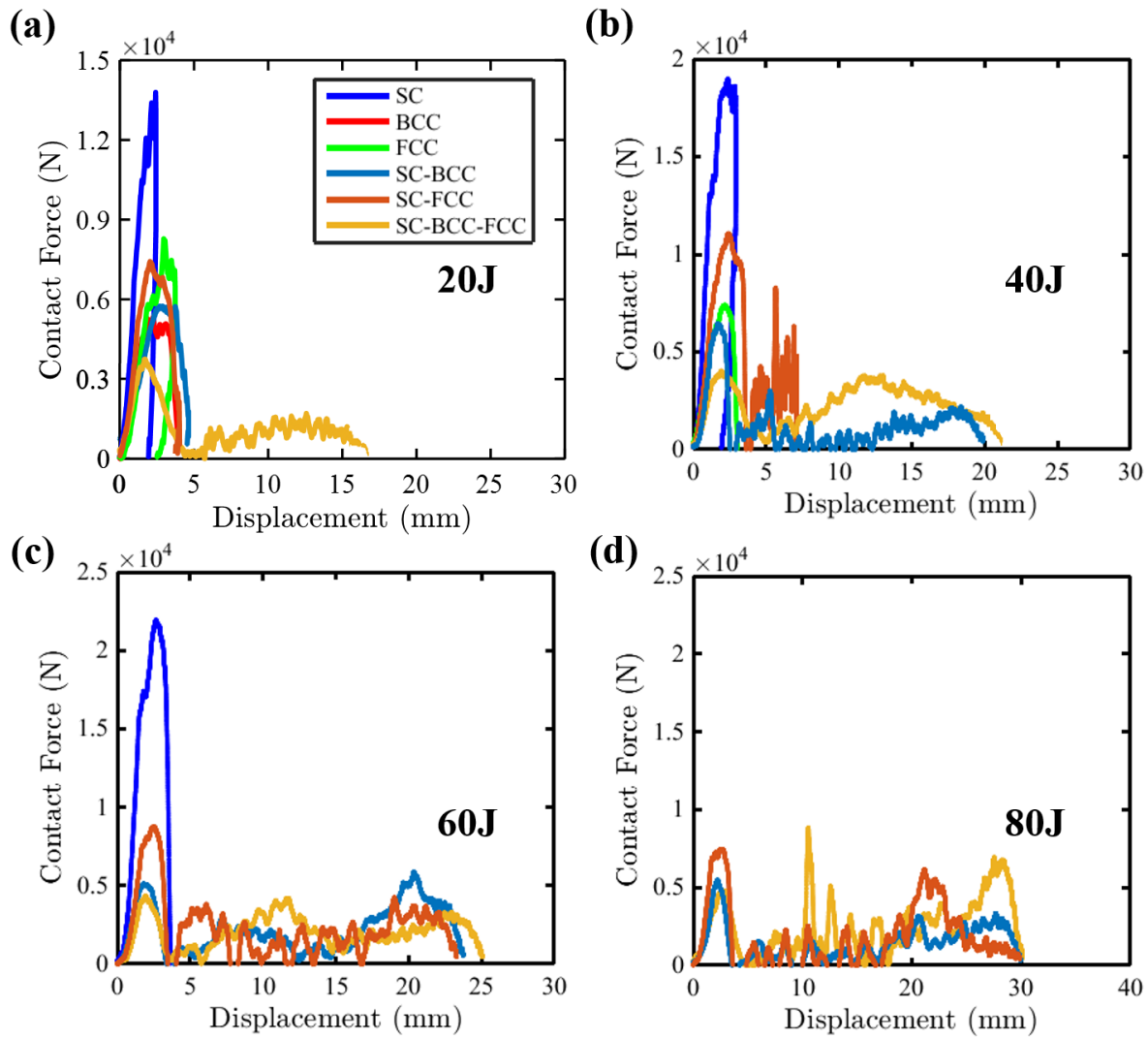
218 **3.1. Effect of the impact energy**

219
220 The dynamic energy absorption characteristics of different 3D plate-lattices were thoroughly
221 investigated to derive useful information for application of such structures in transient impact applications.
222 To study the effect of impact energy, different plate-lattices with the same relative density of 35% were
223 impacted at impact energy levels of 20, 40, 60 and 80 J. Characteristic features of energy-time and load-
224 displacement curves contain useful information for evaluating the damage process of target structures [48-
225 50]. Hence, in this study, such experimental curves are reported as a function of increasing impact energy
226 and plate-lattice topology.

227 The force-displacement and energy-time histories of different plate-lattice specimens are depicted
228 in

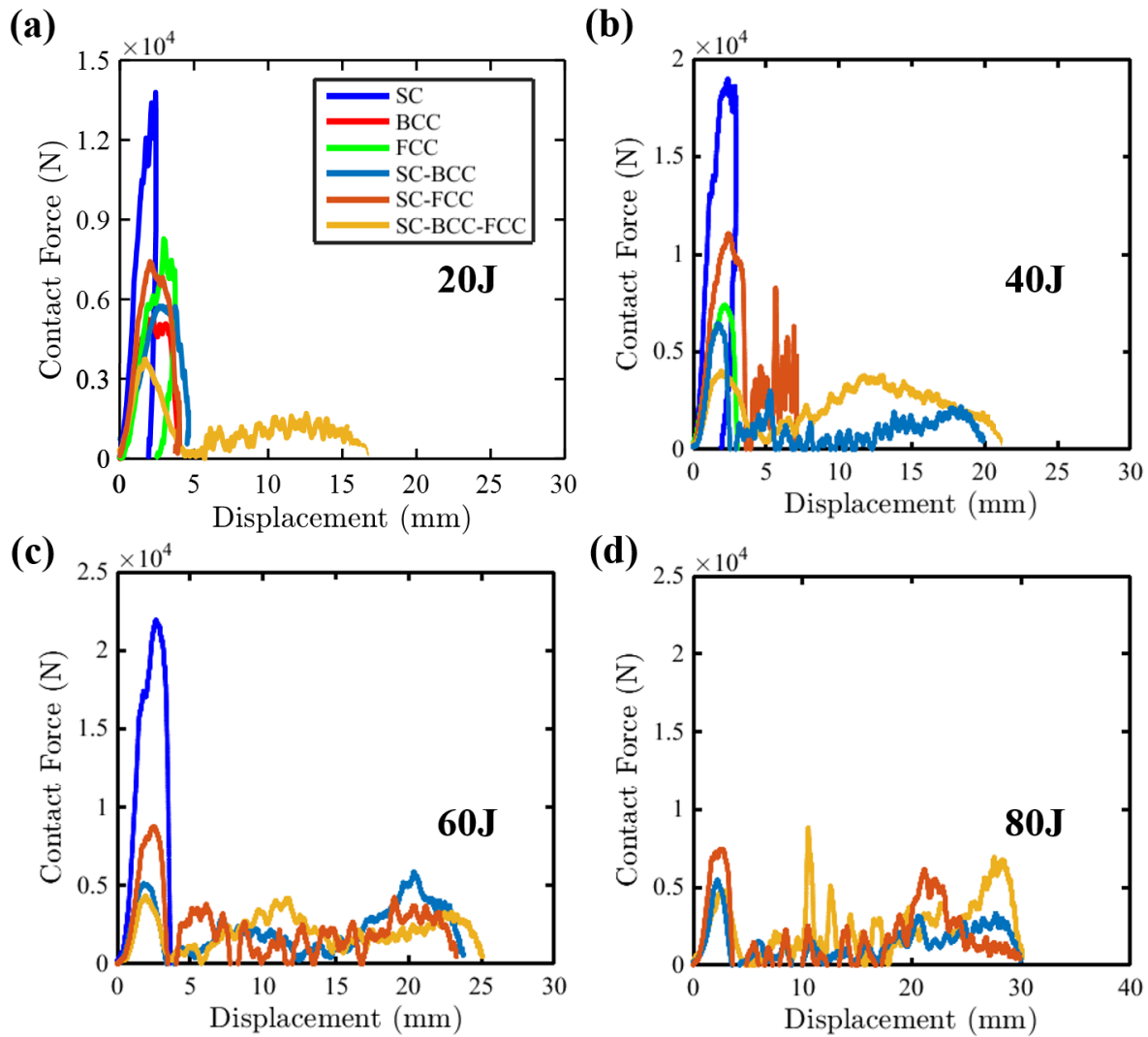


232 [Figure 5](#) and [Figure S1](#), respectively. The experimental curves are depicted up to complete
 233 crushing of the specimens. At impact energy level of 20 J (
 234



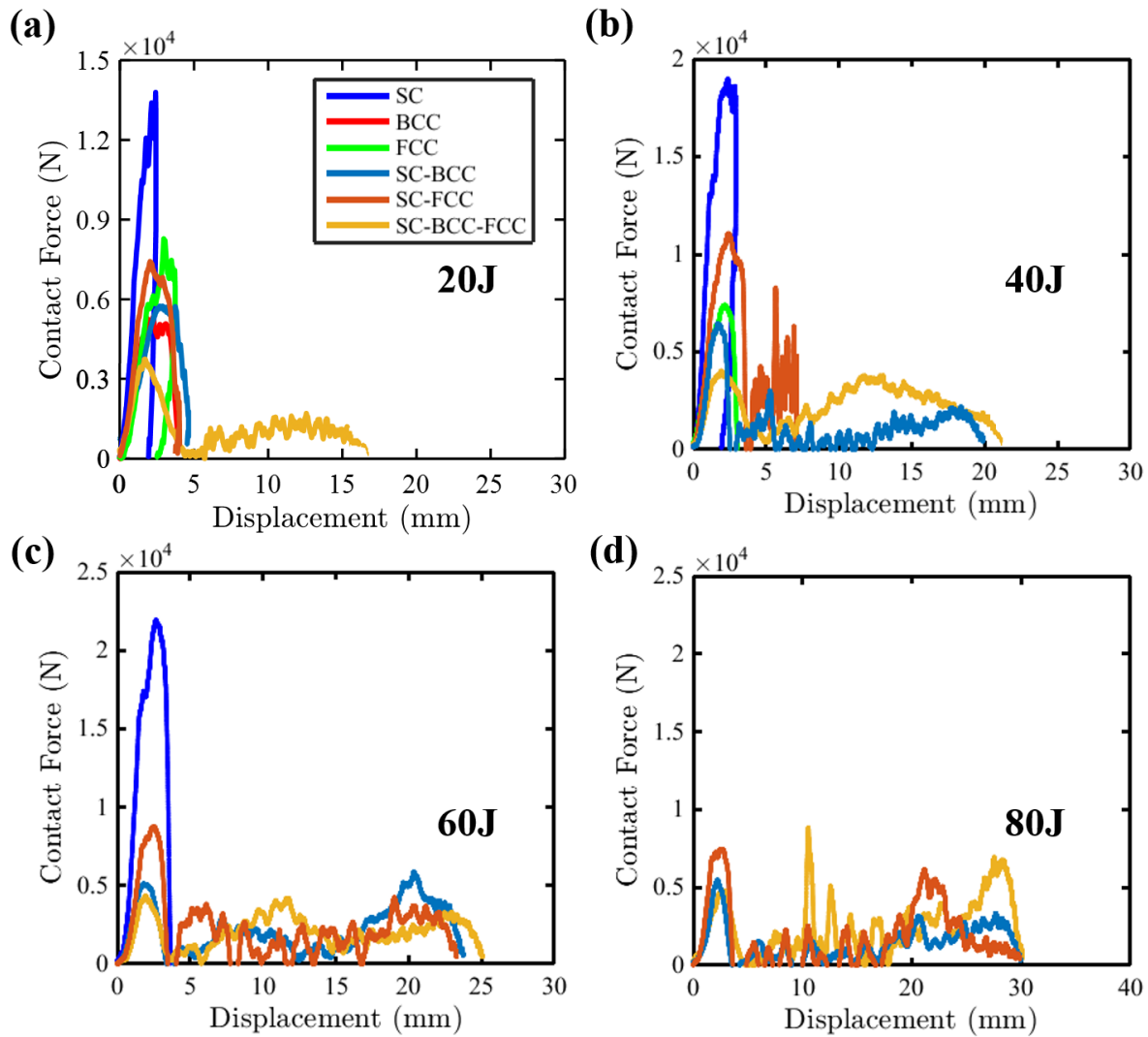
235

236 [Figure 5\(a\)](#), a clear hierarchy in terms of linear stiffness property, i.e. $SC > SC-FCC > SC-BCC-$
 237 $FCC > SC-BCC > BCC > FCC$ is seen (*Table S3*). It can be observed that the ranking order of linear
 238 stiffness and SC volume content among the plate-lattice systems correlate well, as illustrated in



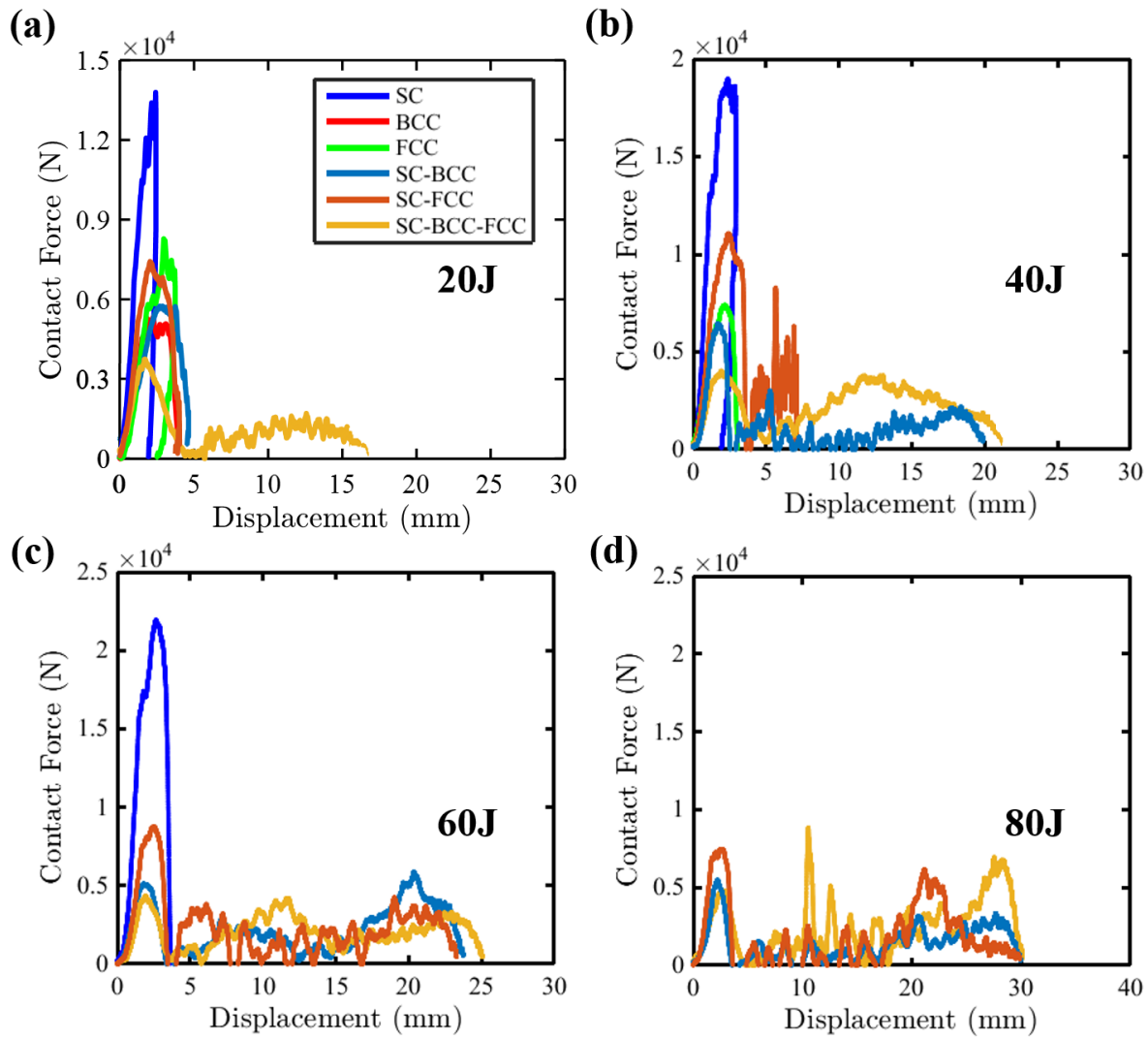
239

240 [Figure 5](#) [Figure-5\(a\)](#) and [Figure 2](#) [Figure-2](#), respectively. It is thus possible that the SC volume content in
 241 the plate-lattice structures could have affected the liner stiffness of the specimens as the stiffest direction
 242 of the SC elementary structure coincides with the loading direction (i.e. high volume of the platelets
 243 coincides with the loading direction, hence stiffest among the plate-lattice structures).



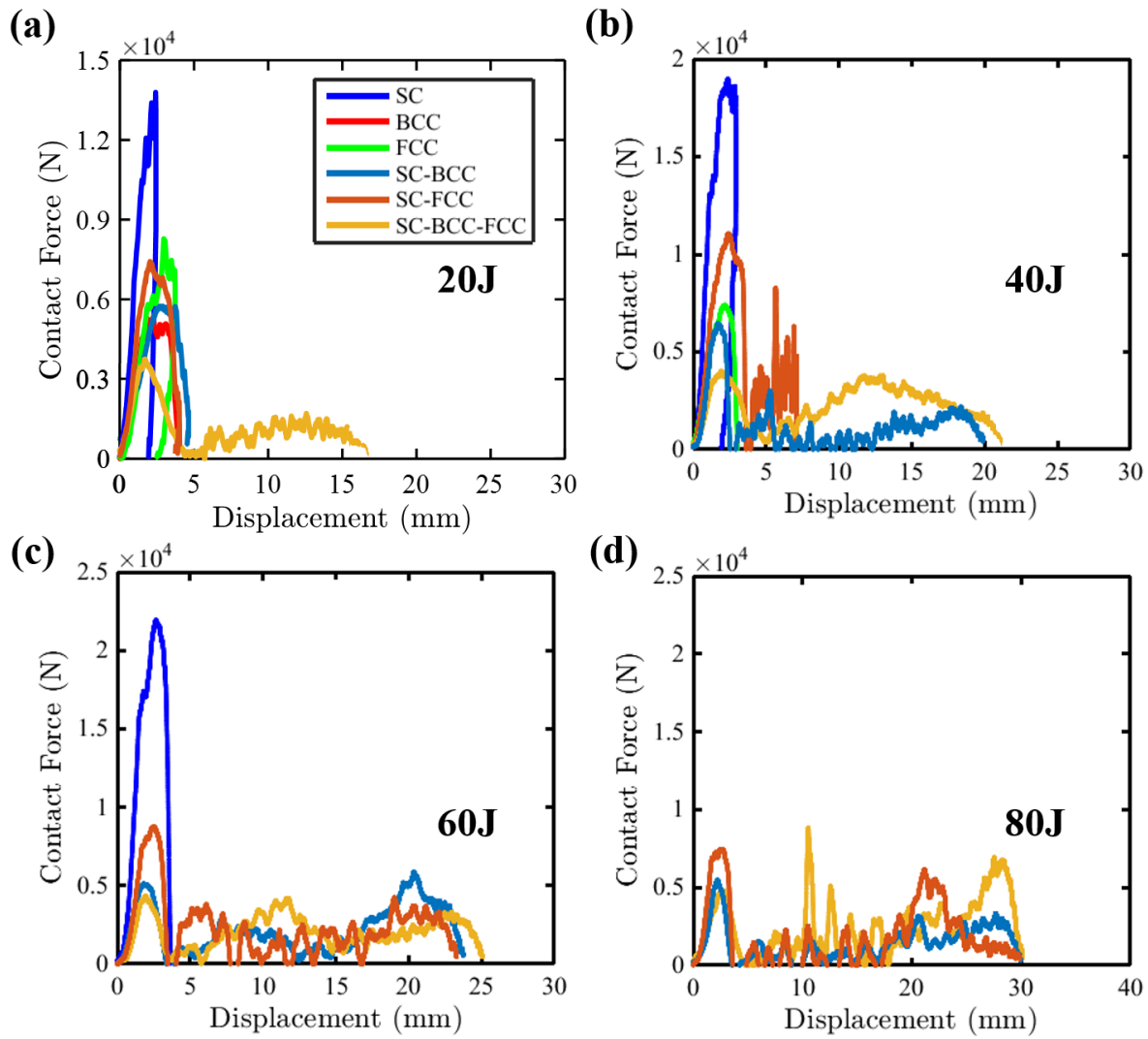
244
 245 Figure 5: Force-displacement curves of different plate-lattices tested at different impact energies: (a) 20 J,
 246 (b) 40 J, (c) 60 J and (d) 80 J.

247 Compared to the linear stiffness, the trend was quite different for peak contact force and absorbed
 248 energy for different plate-lattices. At impact energy of 20 J (



249
 250
 251
 252
 253
 254

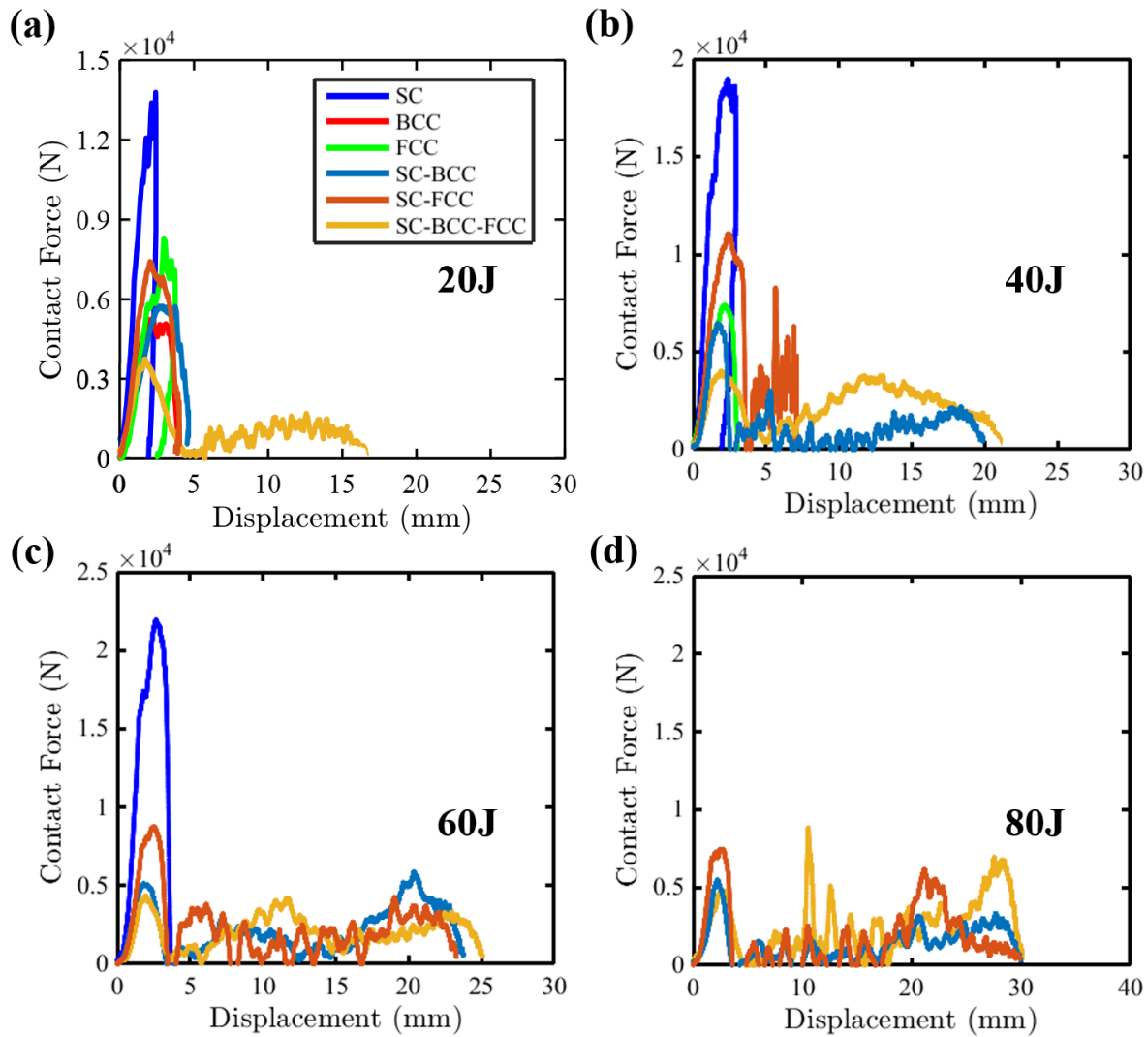
[Figure 5](#)[Figure-5\(a\)](#), BCC lattices were the only specimens that absorbed the impact energy through brittle fracture, whereas all the other specimens showed considerable residual-elastic response or progressive damage growth ([Figure S1](#)). The experimental curves presented suggest that the BCC specimens fully fragmented during the impact test ([Figure 7](#)[Figure-7](#)) after the specimens were crushed by approximately 4 mm (



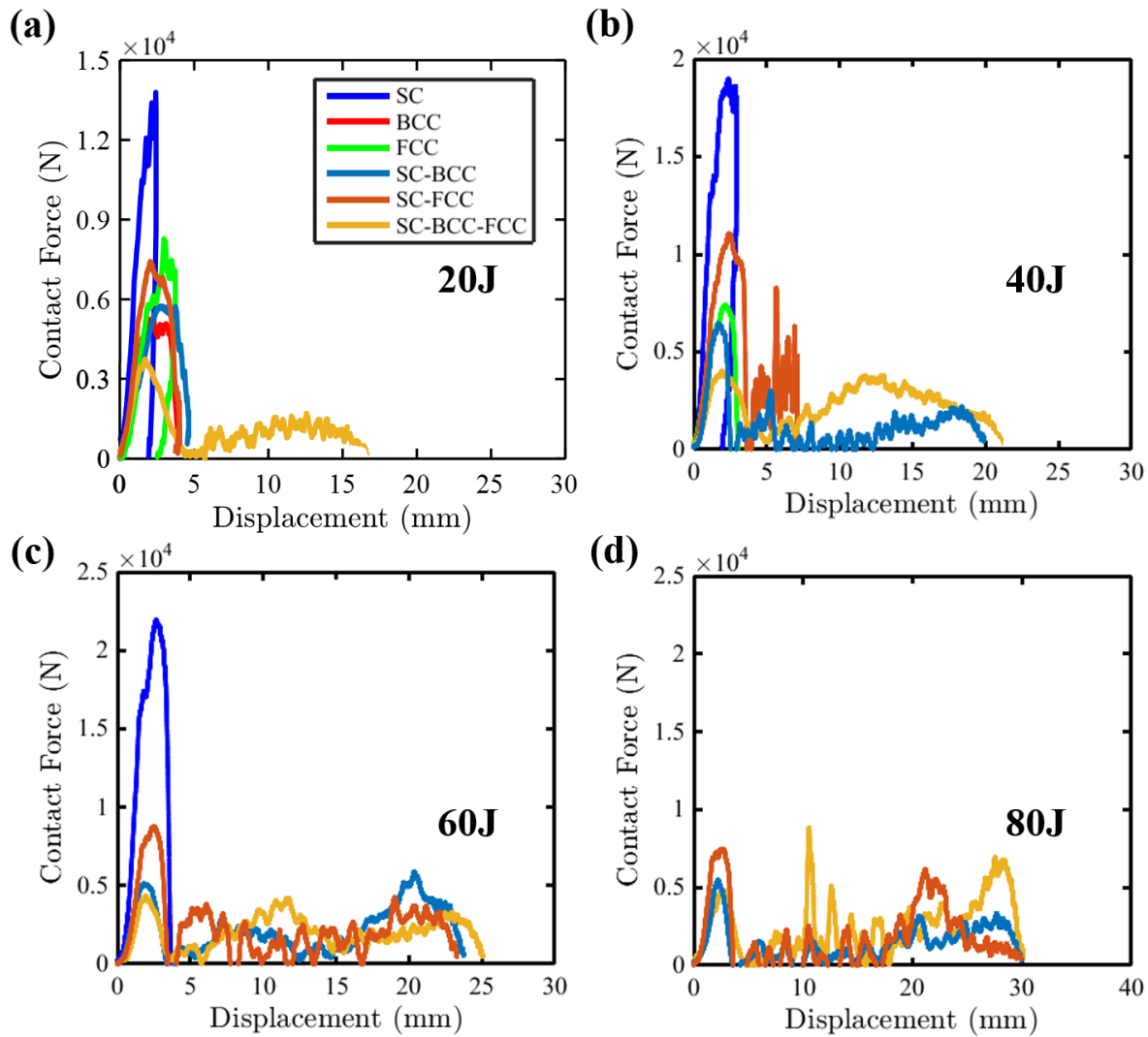
255

256 [Figure 5](#) [Figure 5\(a\)](#) absorbing only about 69% (13.78 J) of applied impact energy ([Figure 6](#) [Figure 6](#)). For

257 the BCC specimens, after the initial peak (



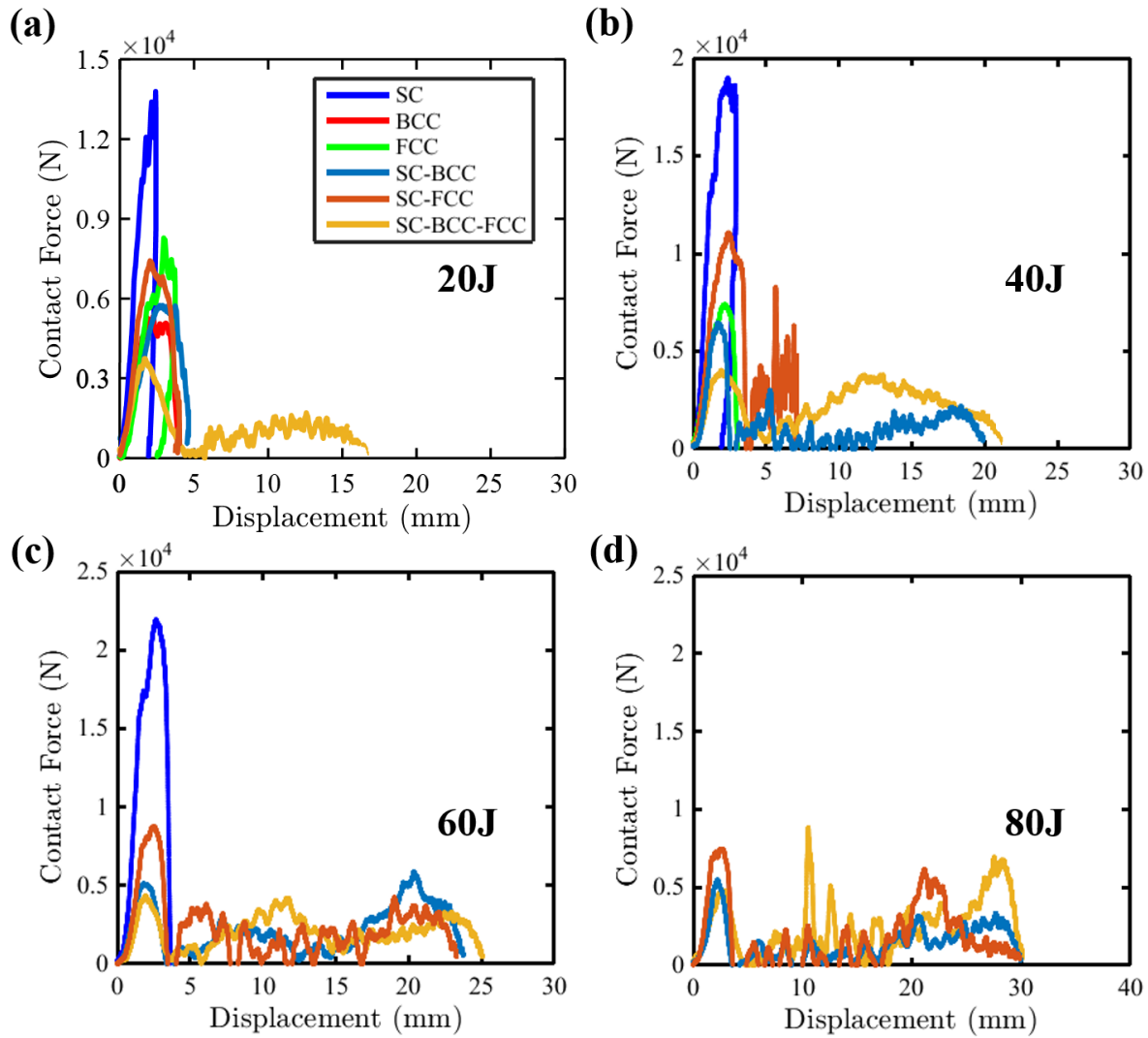
258
 259 [Figure 5](#)Figure 5(a), the pertinent load-displacement curve abruptly dropped to zero. As reported by
 260 several authors, the abrupt drop in a contact force curve right after the initial peak indicates the occurrence
 261 of catastrophic brittle fracture. Moreover, the BCC specimens, despite showing higher initial linear stiffness
 262 compared to the FCC specimens (



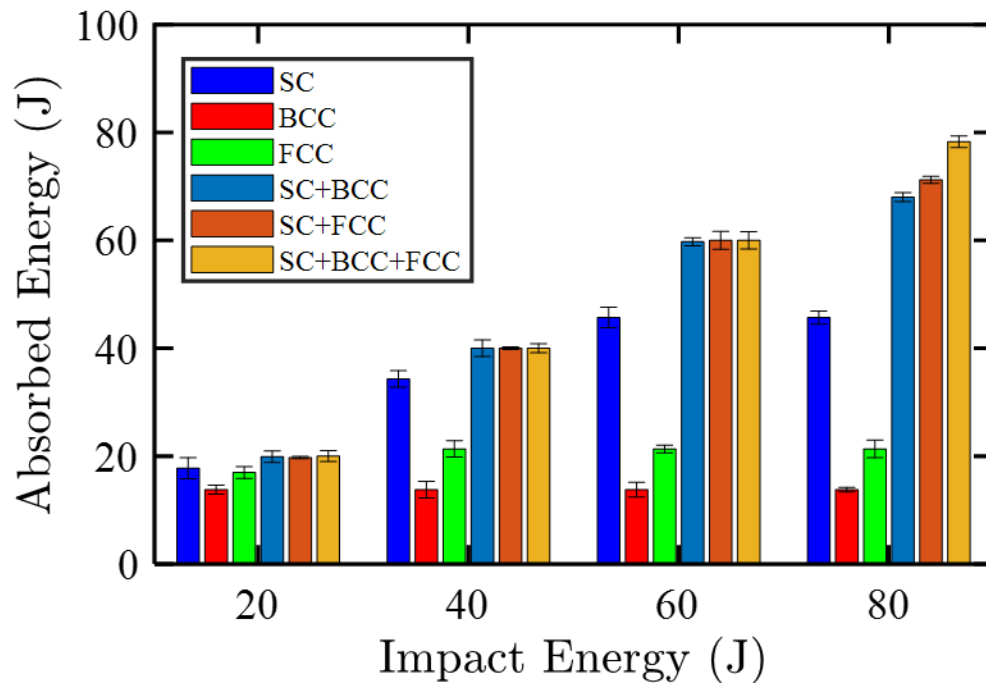
263
 264 [Figure 5](#)[Figure-5\(a\)](#)), exhibited a lower load tolerance. The presence of higher number of stretch dominant
 265 thin walled members (thin walled - due to high surface area distribution among the elementary specimens
 266 – see [Figure 2](#)[Figure-2](#)) in the loading direction might have resulted in the premature brittle failure.

267 The contact force-displacement curves of SC and FCC specimens exhibited a perfect closed pattern
 268 (an elastic rebound phase), as both contact force and displacement reduced almost to the axis origin,
 269 confirming that some elastic energy has been recuperated causing the rebound of the striker. This suggests
 270 that the impact energy was not adequate to induce damage in the specimens ([Figure 7](#)[Figure-7](#)). The
 271 response of SC-BCC and SC-FCC specimens impacted at 20 J showed an incomplete rebound phase. In
 272 contrast, no elastic rebound trait was observed for the SC-BCC-FCC specimens subjected to the same
 273 same impact energy (20 J). The occurrence of some minor damages in the thin walled members of the hybrid
 274 structures ([Figure 7](#)[Figure-7](#)) might have resulted in incomplete rebound or no rebound trait. The
 275 experimental traces for the SC-BCC-FCC specimens remained almost the same (i.e. similarities in the

276 trend) for all the impact energy levels (



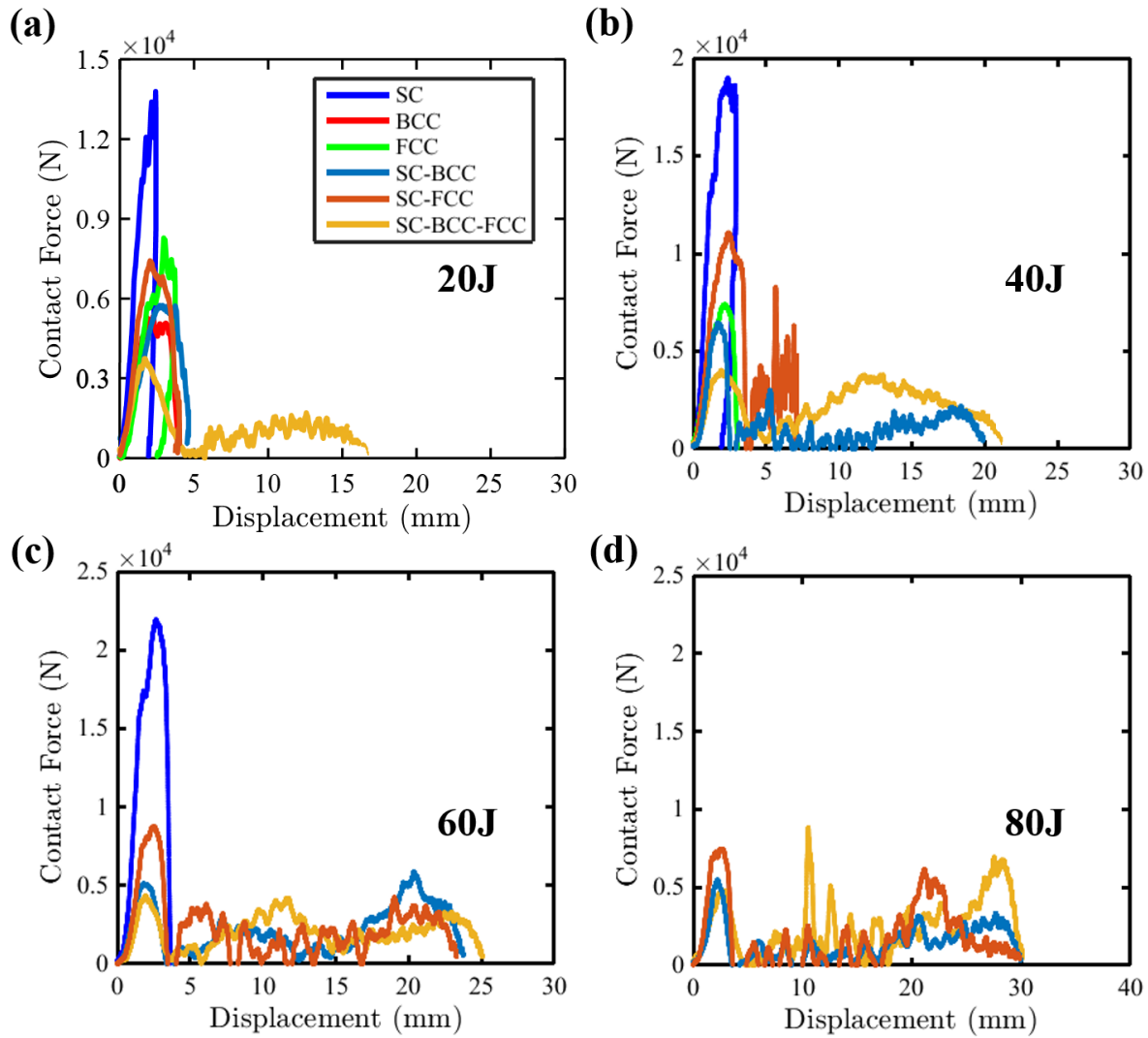
277
278 [Figure 5](#) [Figure 5\(a-d\)](#). SC-BCC-FCC specimens had a long oscillation region and encountered long
279 contact duration ([Figure S1](#)) before reaching the ultimate failure. At all the impact energy levels, the energy-
280 time history progressively increased, until the maximum energy was absorbed.



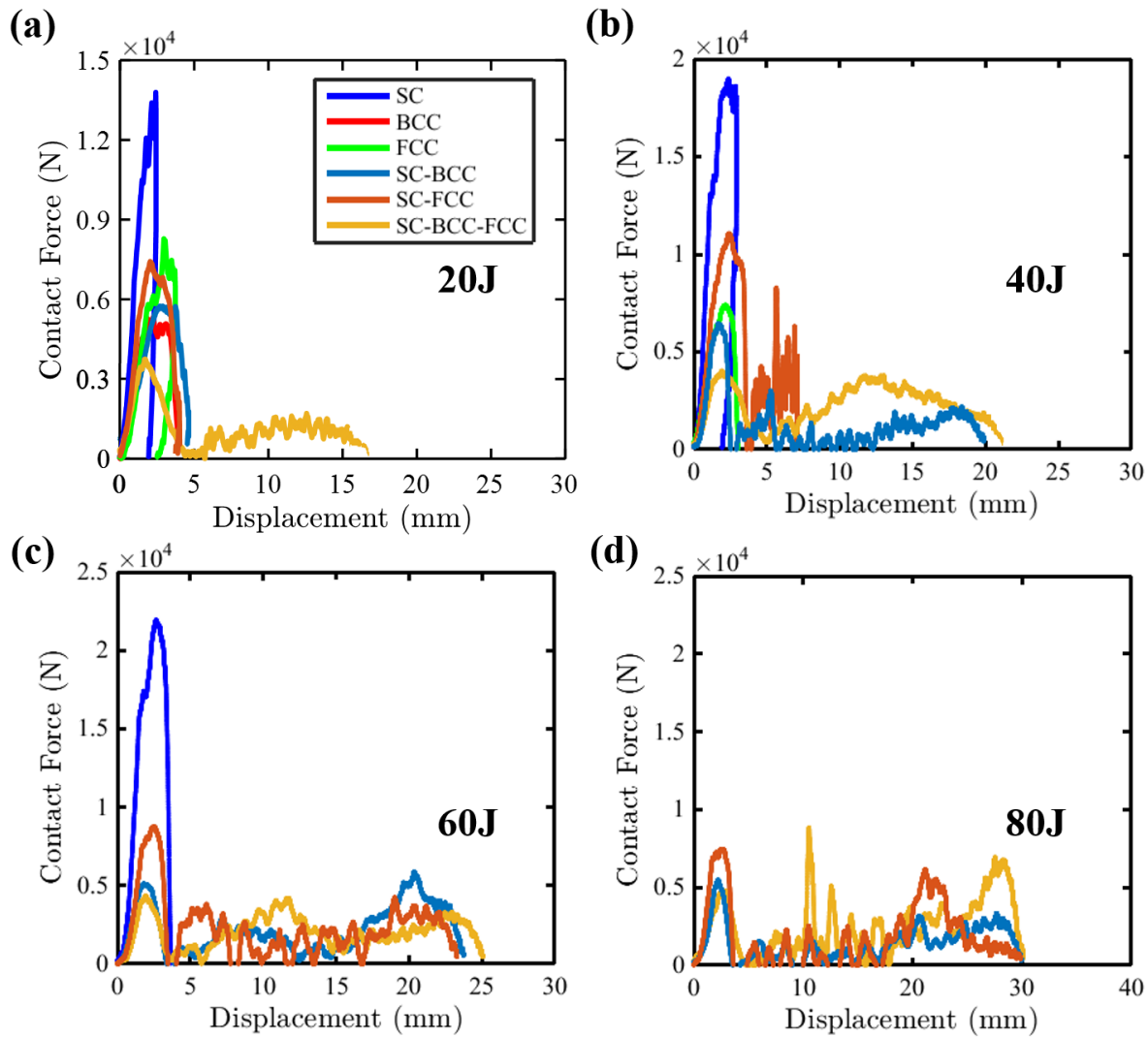
281

282 *Figure 6: Absorbed energy of different plate-lattices tested at various impact energies.*

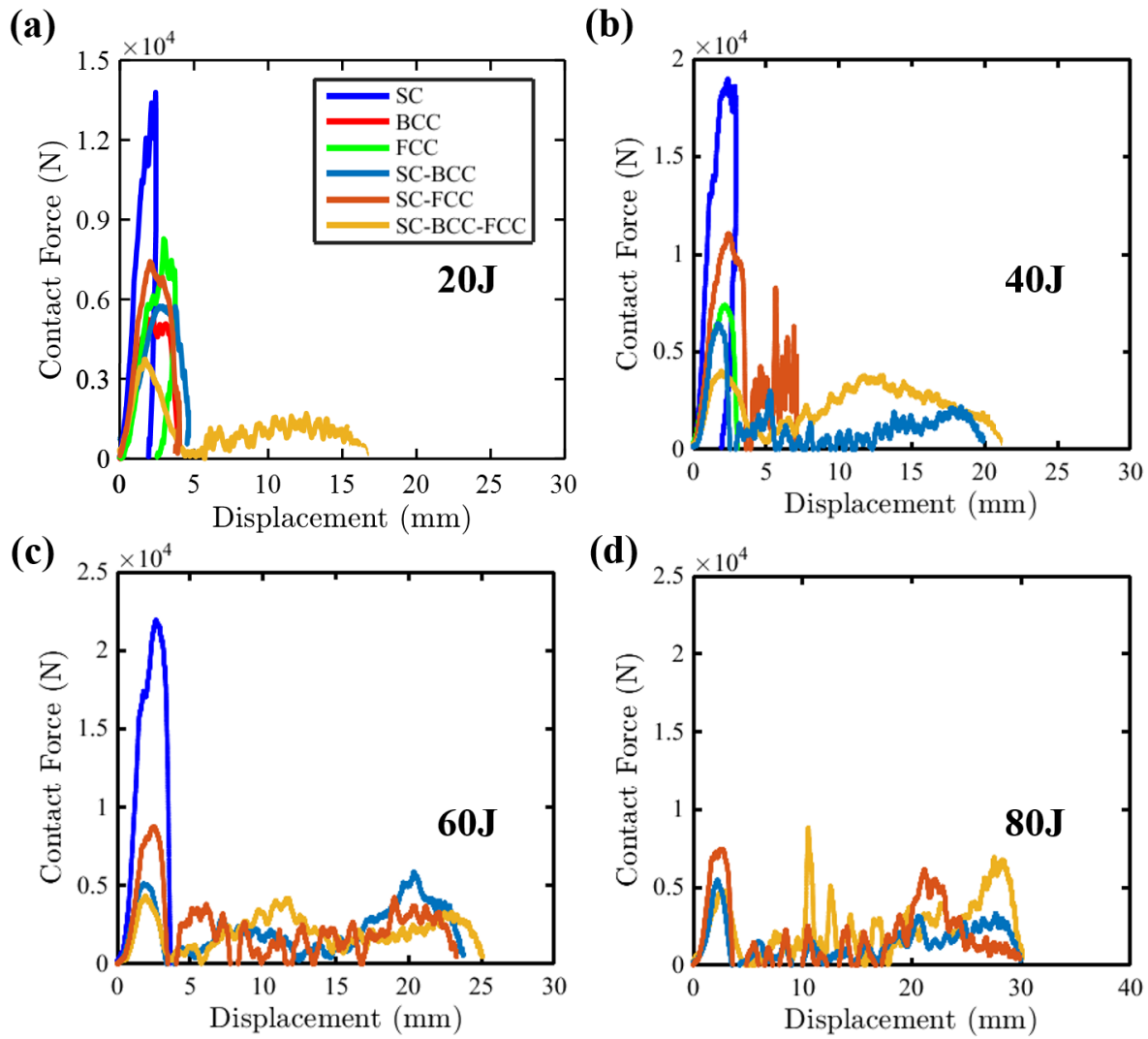
The trends of the initial linear stiffness for different plate-lattice specimens impacted at 40 J (



285 *Figure 5* *Figure 5* (b)) was the same as at 20 J (

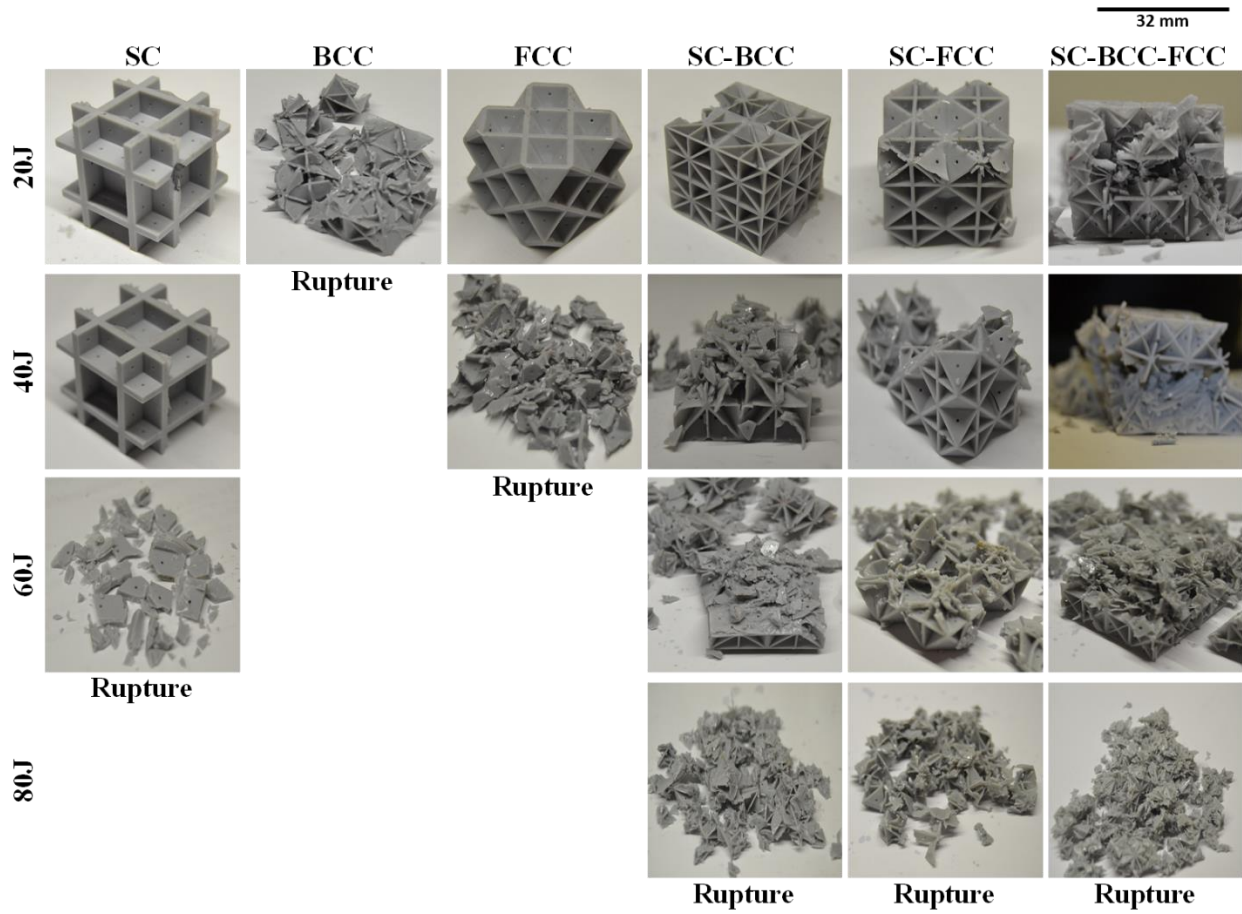


286
 287 *Figure 5(a)*. The FCC, SC-BCC and SC-FCC specimens, in spite of exhibiting elastic rebound
 288 behavior at 20 J, showed a substantial change in terms of energy absorption and contact force-displacement
 289 trait at 40 J. The FCC specimens exhibited catastrophic failure by brittle fracture. The energy-time curves
 290 of SC-BCC and SC-FCC specimens impacted at 40 J exhibited a short initial plateau region at 14.17 and
 291 28.81 J, respectively (*Figure S1*). As reported by numerous authors [48], the initial short plateau region in
 292 the energy-time history of SC-BCC and SC-FCC specimens indicates the occurrence of major damage.
 293 Also, the force-displacement curves of these specimens showed an open pattern (



294

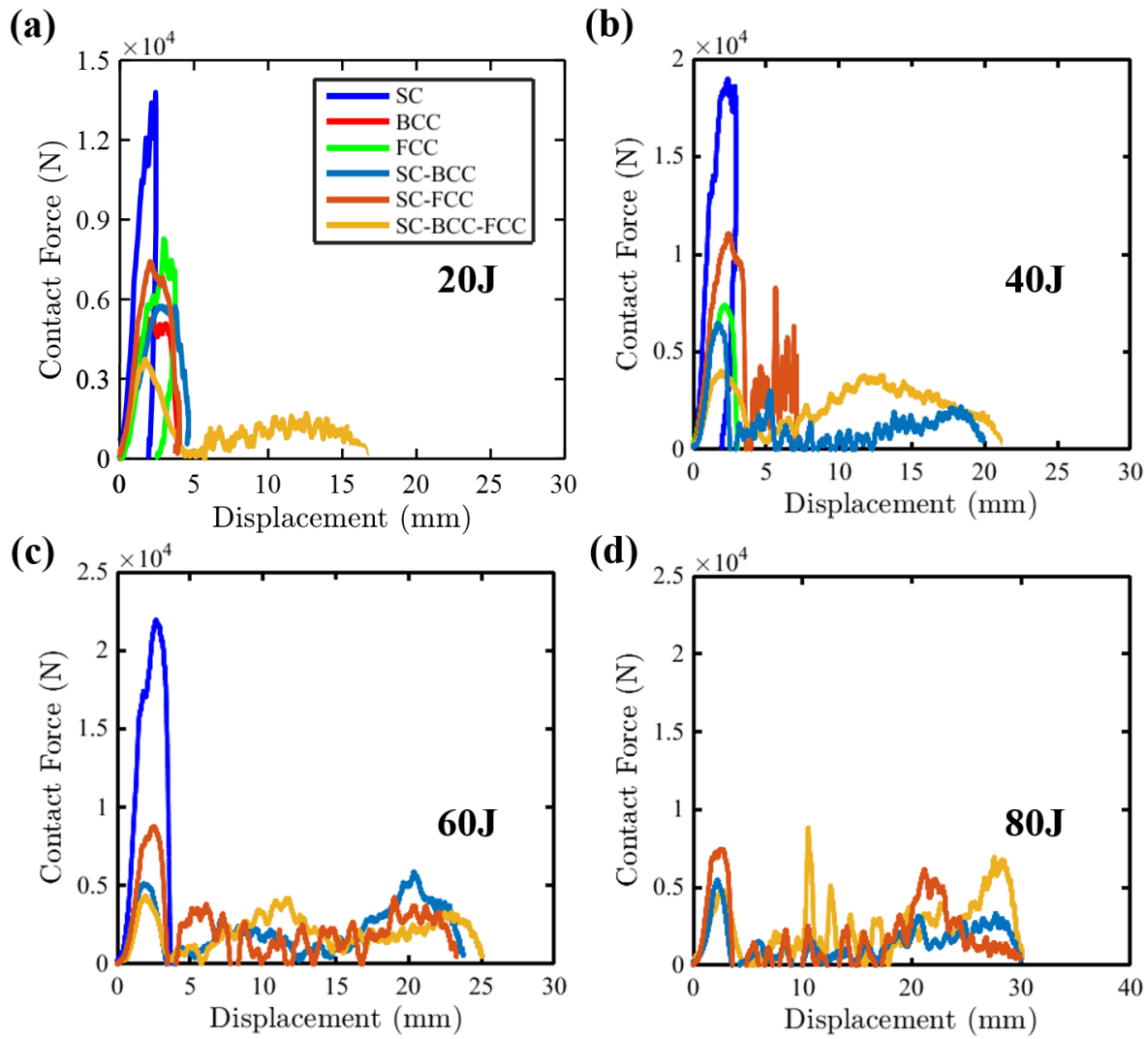
295 [Figure 5\(b\)](#)), confirming that some impact energy was absorbed causing the damage. Similar
 296 suggestions can be drawn for SC-BCC-FCC specimens.



297

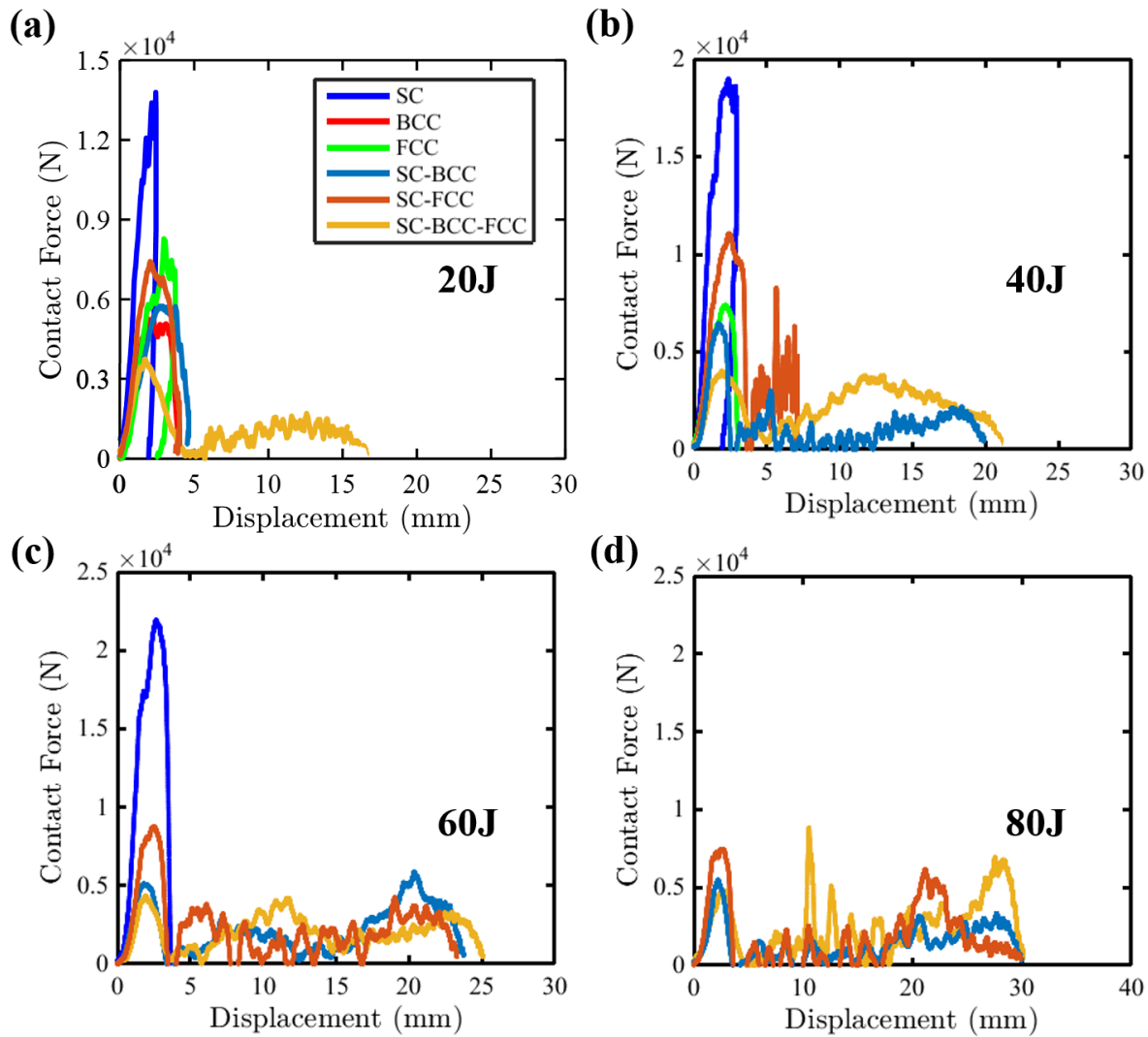
298 Figure 7: Post-test photographs of different plate-lattice specimens tested at various impact energies.

299 Up to 40 J, no visible damage was noticed for SC specimens and the impactor rebounded with an
 300 energy of 5.69 J. The SC specimens, despite showing the highest initial linear stiffness compared to the
 301 other plate-lattice specimens (*Figure 5(a)*), exhibited a premature brittle failure at an impact energy of 60
 302 J (



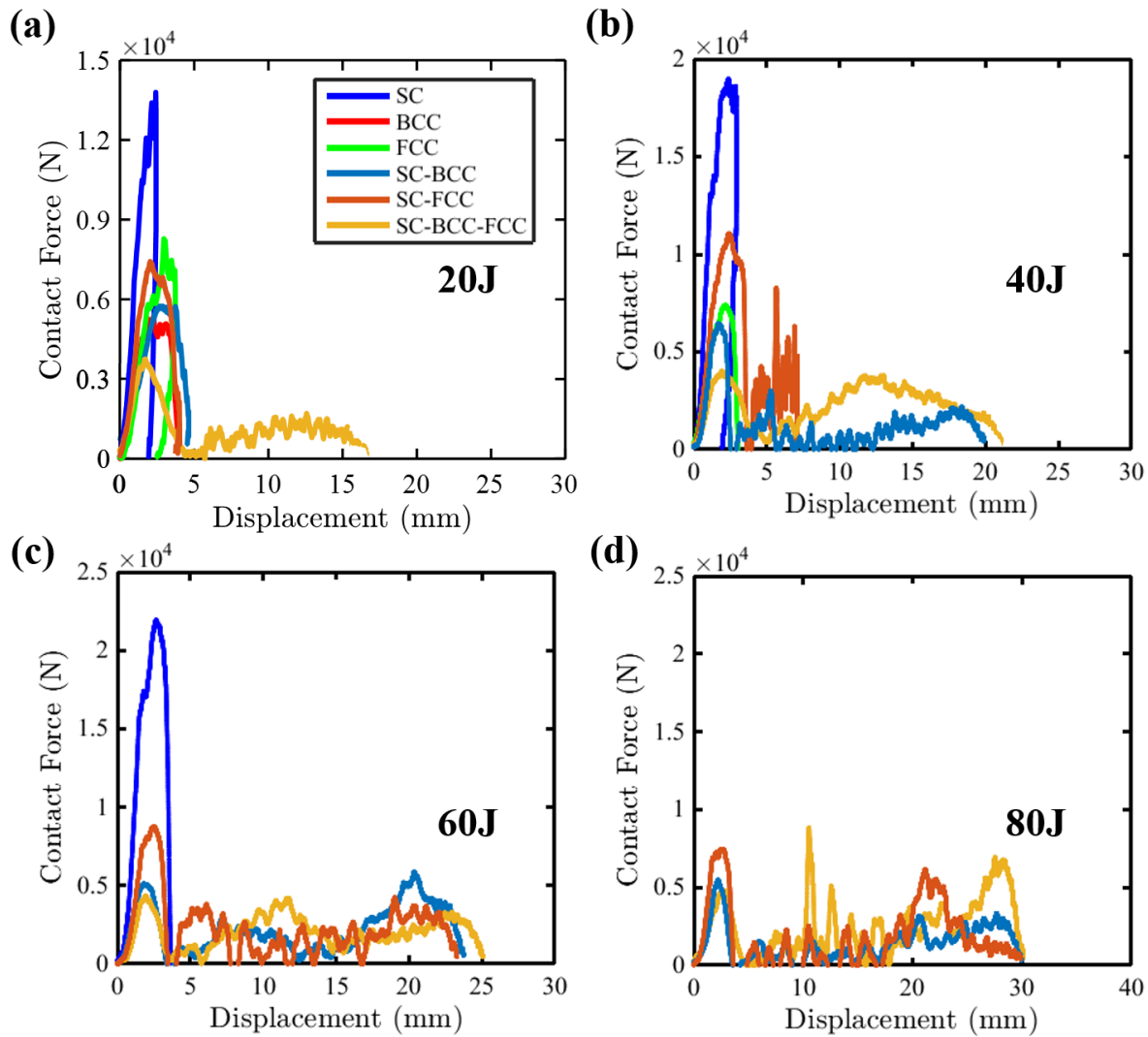
303

304 [Figure 5\(c\)](#). SC specimens completely fragmented at 46.49 J devoid of exhibiting any energy
 305 recovery (



306
 307 *Figure 5(a)* [51], while all the other hybrid specimens comprising both stretch and bending
 308 dominated constituent plates [12] showed a progressive damage growth. Even though the SC elementary
 309 specimens have the highest volume of plates coinciding with the loading direction compared to the other
 310 specimens, the absence of bending dominant plates [12], responsible for restricting transverse buckling
 311 (like in other specimens), might have resulted in premature fracture.

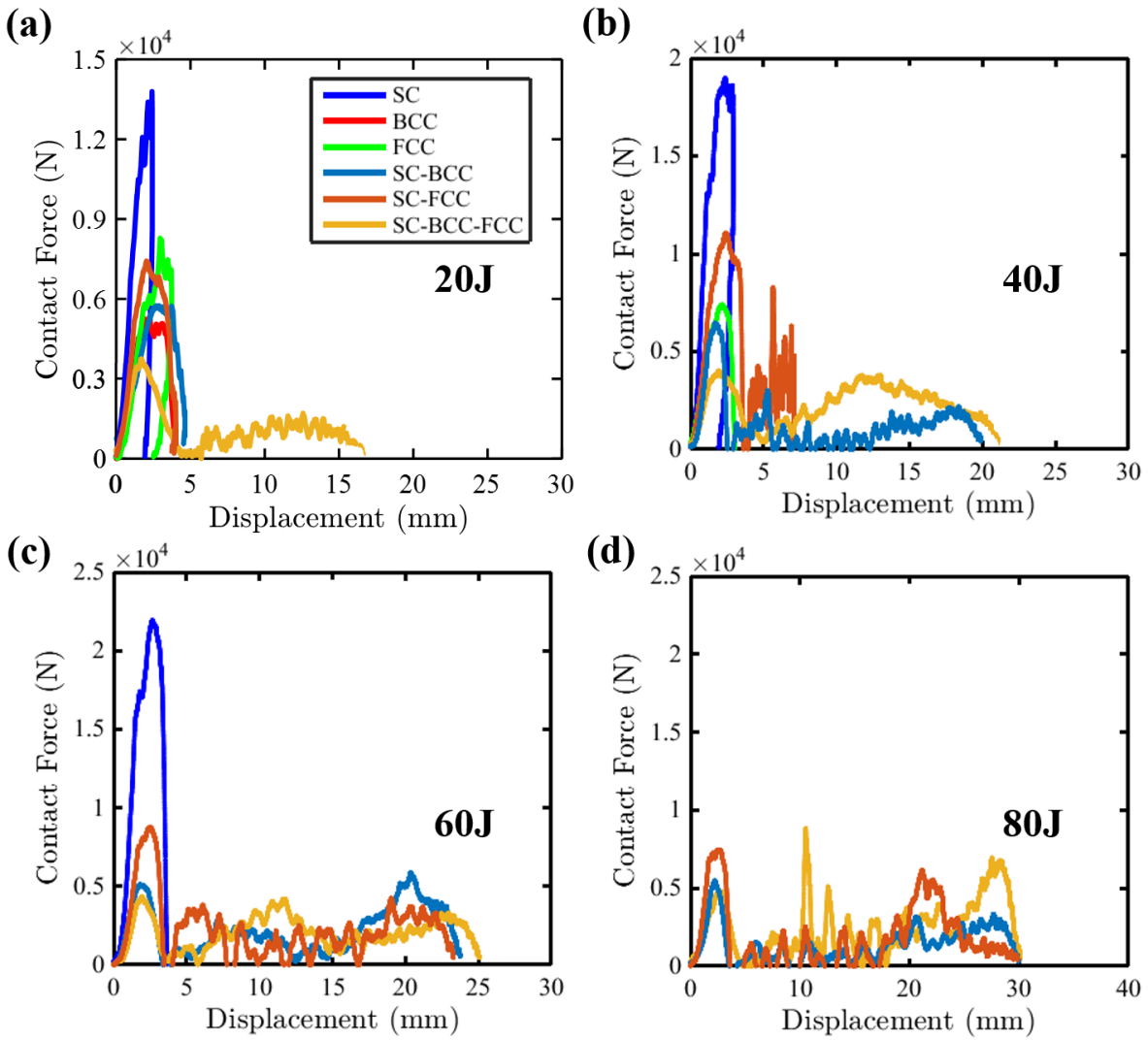
312 As revealed by measured responses, the plate-lattice configuration heavily influenced the energy
 313 absorption behavior, with hybrid structures outperforming elementary ones, progressively as the impact
 314 energy raises (



315
 316 *Figure 5(a-d)*. As indicated, SC specimens performed better compared to the other configurations
 317 up to an impact energy of 40 J. At higher energy levels (> 40 J) the trend changed for the hybrid specimens
 318 which outperformed SC ones. After the peak contact force was reached, the contact force-displacement
 319 curve reduced by following almost a non-oscillating and linear fashion at 60, 20 and 40 J for SC, BCC and
 320 FCC specimens, respectively. These experimental results overall confirm the poor energy absorption
 321 property of all the elementary plate-lattice structures. After the initial peak, the load-displacement curves
 322 of SC-BCC, SC-FCC and SC-BCC-FCC specimens went up with a long irregular plateau with several
 323 oscillations. These oscillations are usually attributed to the development of the progressive localized
 324 damages [52]. It was obvious that the area under the force-displacement curves increased with the impact
 325 energy level, signifying a raise of absorbed energies and damages in the specimens. As a result, these
 326 structures dissipate a huge amount of impact energy. As reported by Tancogne et al. [12], the softest
 327 direction of the BCC and FCC elementary structures coincides with the stiffest direction of the SC

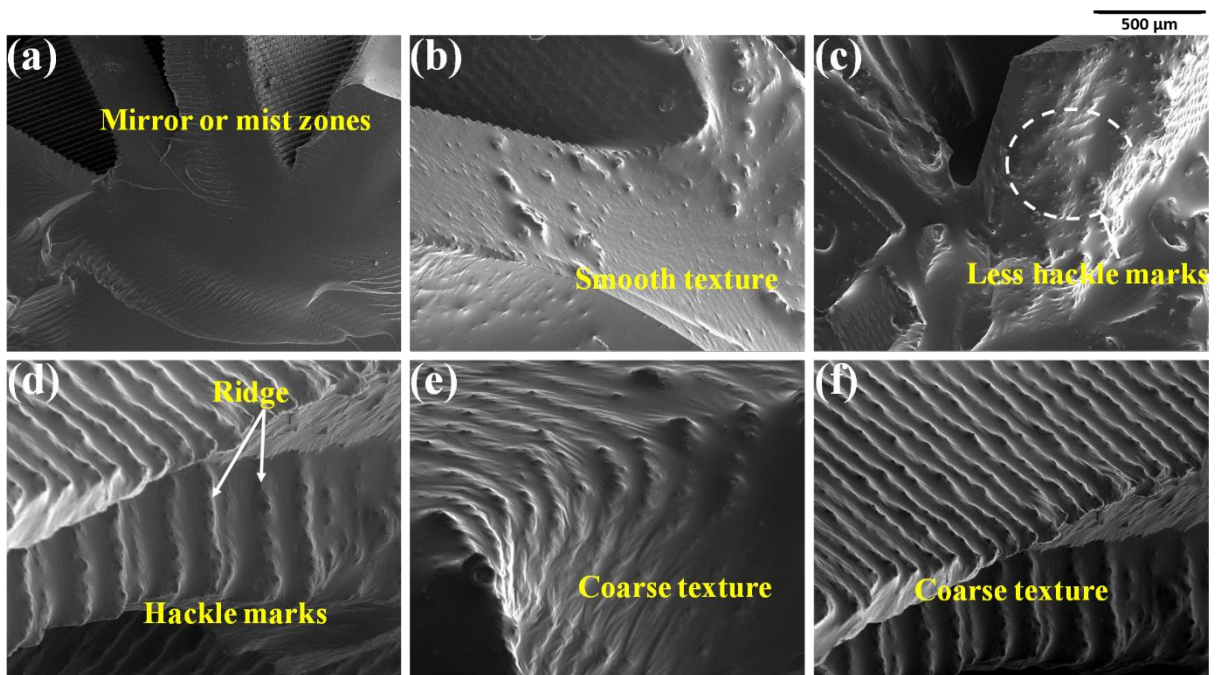
328 elementary structure, and vice versa. Hence, each constituent plate-lattice in the SC-BCC-FCC lattice
 329 structure contributes to the impact performance. Moreover, it is reasonable to suggest that the existence of
 330 a larger number of repeated open and closed sub-cells in the SC-BCC-FCC structure might have resulted
 331 in delaying the premature failure of the lattice structures by more effectual impact damage redistribution as
 332 reported in other investigations on various cellular lattice structures [53].

333 Not only do the impact properties of the six plate-lattice structures vary, the damage mechanisms
 334 and deformation processes vary as well. The deformation process has a direct link with the configuration
 335 of the plate-lattice structure. *Figure 7* illustrates the damage profiles of various plate-lattice
 336 specimens. Compared with the elementary specimens, hybrid specimens showed distinct damage
 337 characteristics. From the



338 *Figure 5(a-d)* and *Figure 7* it is apparent that the maximum displacement to the failure of
 339 the hybrid specimens was considerably higher than that of the elementary ones. Specifically, after being
 340

341 crushed to a displacement of 3.52, 3.88 and 3.01 mm, the SC, BCC and FCC specimens absorbed about
 342 45.69, 13.78 and 21.34 J of the applied impact energy, respectively and showed abrupt and catastrophic
 343 brittle failure. These observations indicate that the cracks developed up to the striker displacement of 3.52,
 344 3.88 and 3.01 mm (i.e. 11%, 12.125% and 9.40% of the specimen height), respectively, abruptly advanced
 345 through the whole specimens, leading to ultimate failure. In contrast, for the hybrid specimens ([Figure](#)
 346 [7](#)) (especially for the SC-BCC-FCC specimens), certain portions of the cellular structures stayed
 347 intact even after the striker was in contact with the specimens for a larger displacement (~23 mm) and
 348 longer contact duration (~14 ms). These results indicate that the hybrid specimens greatly restricted the
 349 damage propagation and diffused the impact load (progressive damage growth).



350
 351 *Figure 8: Post-mortem SEM micrographs for (a) SC, (b) BCC, (c) FCC, (d) SC-BCC, (e) SC-FCC and (f)*
 352 *SC-BCC-FCC specimens.*

353 [Figure 8](#) illustrates the SEM micrographs of different plate-lattices after drop-weight
 354 impact tests. In the elementary structures (specifically SC specimens), radiating stress crack signatures,
 355 known as hackle marks, were fewer spotted. Evident signs detected suggest the presence of mirror or mist
 356 areas in the fractured surface. Such signatures are regarded as smooth fracture surfaces, and are revealing
 357 unstable crack growth [4, 54]. Analysis of the surface of hybrid structures, as depicted in [Figure 8](#)
 358 (d-f), revealed many obvious hackle signs. The presence of chevron markings, else known as a plumose
 359 pattern, characterizes the development of hackle marks. The plumose pattern comprises alternating
 360 arrangements of ridges detached by smooth surface regions (concentric rings). Further, the distance between

361 the concentric ridges increased gradually away from the origin of the crack. These signatures were thought
362 to represent progressive crack propagation (characteristic of slow crack growth) by alternating series of
363 cracking and stoppage. The increase in distance between the adjacent ridges with increasing distance from
364 the crack origin supports this conclusion, and is commonly observed in other progressive failure profiles
365 [54]. This suggests why hybrid structures perform better than elementary ones, in terms of impact energy
366 absorption.

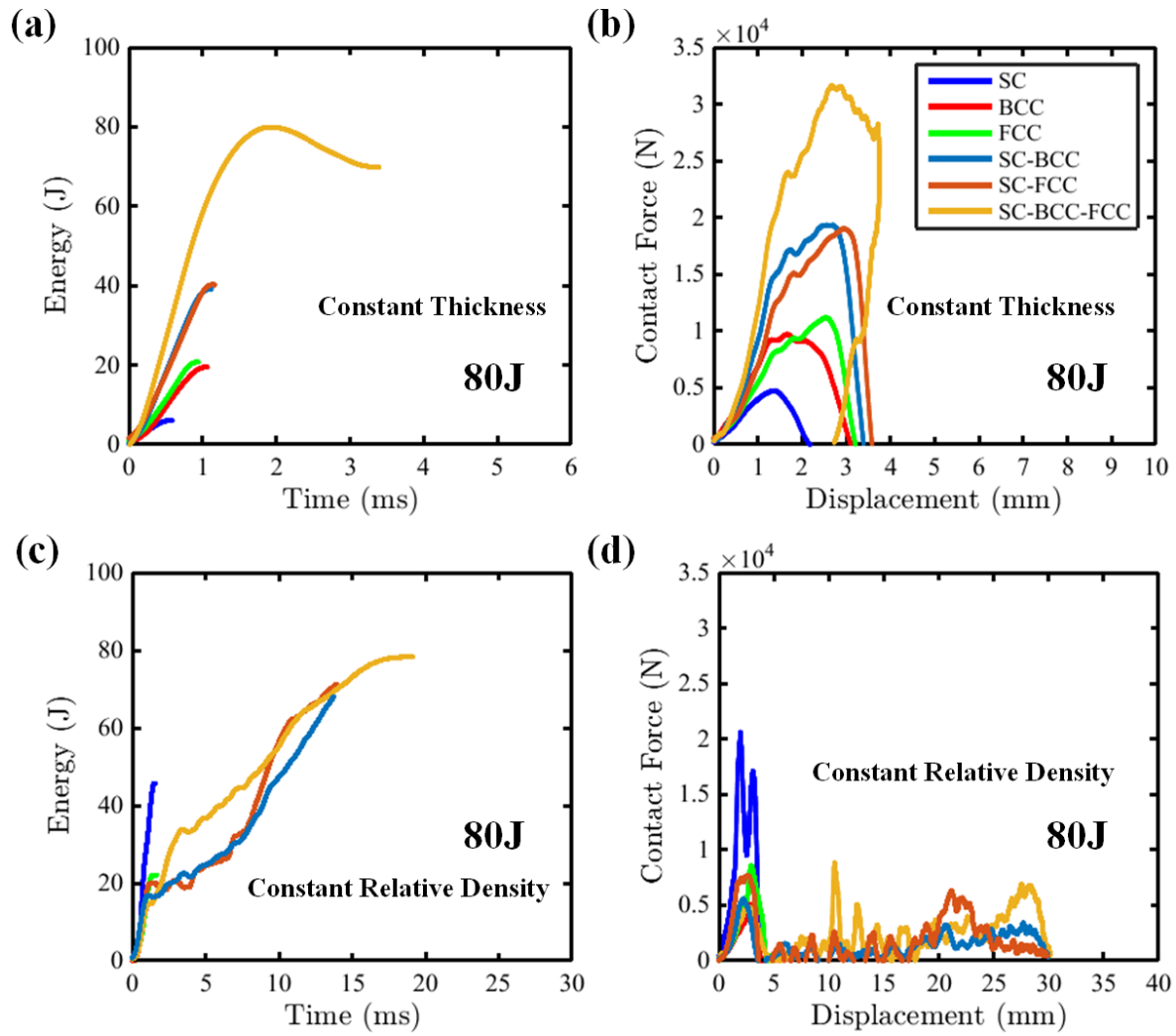
367 **3.2 Constant plate thickness vs. constant relative density**

368 The low velocity impact tests were performed on two sets of six different plate-lattice specimens,
369 by keeping the relative density constant at 35% for one set and by keeping the plate thickness of the
370 individual unit cells constant at 1 mm for another set at an impact energy of 80 J. Their energy-time and
371 load-displacement curves are illustrated in [Figure 9](#). The main interest behind comparing the
372 constant thickness and constant density specimens is to qualitatively examine how the thickness distribution
373 of different elementary structures influences the deformation profile pertinent to the energy absorbing
374 mechanism. Since the relative density for both categories of specimens was different, qualitative
375 comparison between constant relative density and constant thickness specimens was made initially through
376 the analysis of the trends in measured response.

377 From the low velocity impact tests carried out on the different constant thickness specimens it is
378 apparent that a clear hierarchy in terms of absorbed energy was observed ([Figure 9\(a\)](#)), i.e. SC-
379 BCC-FCC > SC-FCC > SC-BCC > FCC > BCC > SC. It can be noted that the ranking order of absorbed
380 energy and relative density between the plate-lattice systems correlate well, as depicted in [Figure 9](#)
381 (a) and [Figure 2](#), respectively. It is, as a result, possible that the relative density can influence
382 the energy absorption of the specimens. The force-displacement curves of these specimens (except for SC-
383 BCC-FCC) exhibited a sudden drop right after the peak contact force, signifying that the complete rupture
384 was occurred (see [Figure 9](#) (b) and [Figure 10](#)), devoid of rebound. In contrast, for the
385 SC-BCC-FCC specimens, the load-displacement history had a single peak and trailed with a considerable
386 rebound at the end of the impact event with an almost enclosed profile. In order to evaluate the toughness
387 and ultimate deformation pattern, the SC-BCC-FCC specimens were subjected to impact at a higher impact
388 energy of 150 J. Here, the experimental curves and deformation pattern (see [Figure S2](#)) seem to have the
389 same profile as that of the constant wall-thickness specimens, highlighting abrupt brittle fracture at an
390 absorbed energy of 110 J.

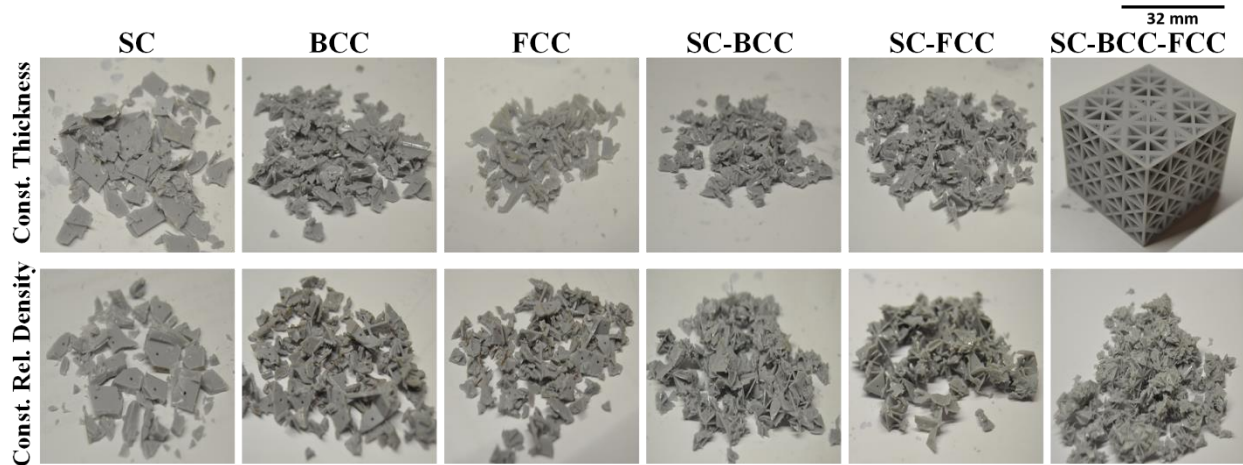
391 The trend of the impact energy absorption was partially altered for the constant relative density
392 specimens, as shown in [Figure 9](#) (c-d). All the configurations with constant relative density can be
393 ordered from the lower to the higher impact energy absorption as followed ([Figure 9\(c\)](#)): SC-BCC-

394 FCC > SC-FCC > SC-BCC > SC > FCC > BCC. Here, SC specimens surpassed FCC and BCC specimens
395 in terms of absorbed energy. This might be due to the higher thickness of the vertical plates in the SC
396 specimens (see [Figure 2](#)~~Figure 2~~). However, it can be observed that the energy-time and load-displacement
397 traces of SC specimens with constant relative density (even though having a high relative density, see
398 [Figure 2](#)~~Figure 2~~) were comparable to that of the other constant thickness counterparts. Similar
399 observations can be drawn for BCC and FCC specimens. In contrast, for all the hybrid specimens with
400 constant relative density, the structures deformed in a progressive manner, where the contact force ([Figure](#)
401 [9](#)~~Figure 9~~(d)) raised to a maximum value; after the peak point, the contact force dropped intensely to a
402 lower plateau level, followed with a steady- and long-oscillating curve attributable to the plastic
403 deformation of plate walls with wrinkling and fracture. In specific, the peak impact stress transmitted to the
404 specimens were attenuated and significantly extended the duration of the load pulse. Particularly, in the
405 case of the SC-BCC-FCC specimens with a constant relative density, the peak contact force was reduced
406 to about 73% of that encountered in the corresponding constant thickness ones, whereas the contact duration
407 was increased by about 81%.

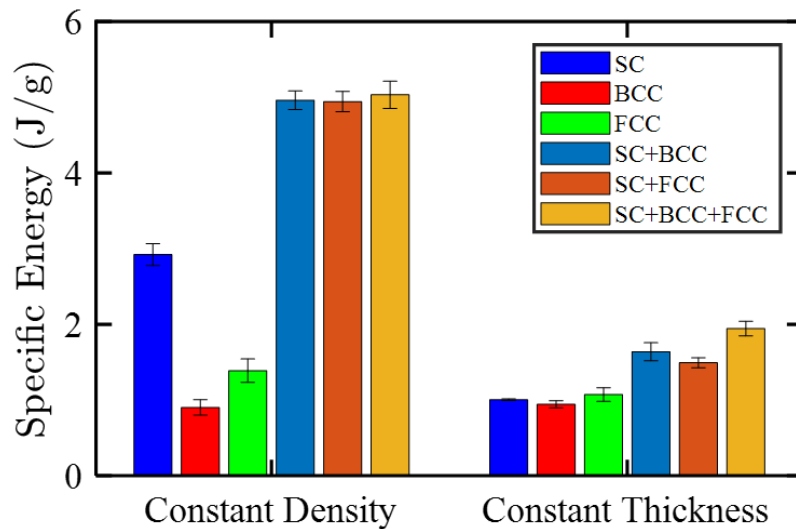


408

409 *Figure 9:* (a) Energy-time and (b) contact force-displacement curves of constant thickness specimens ($t =$
 410 1 mm), and (c) energy-time and (d) contact force-displacement curves of constant relative density
 411 specimens ($\bar{\rho} = 35\%$).



412
 413 *Figure 10: Post-test photographs of different plate-lattice specimens with constant-thickness ($t = 1$ mm)*
 414 *and -relative density ($\bar{\rho} = 35\%$).*



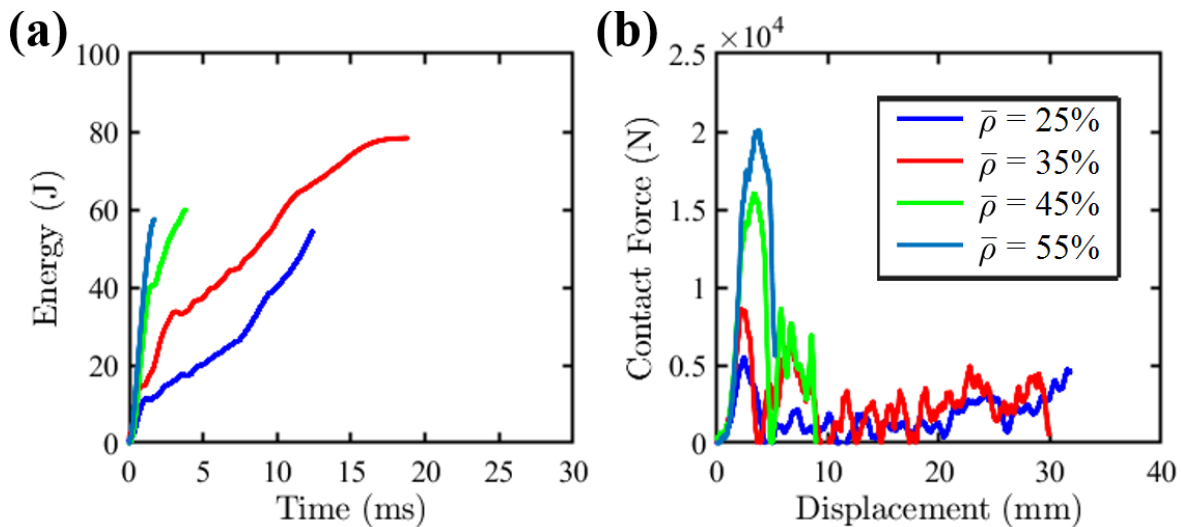
415
 416 *Figure 11: Specific absorbed energy absorption of different plate-lattice specimens with constant-relative*
 417 *density ($\bar{\rho} = 35\%$) and -thickness ($t = 1$ mm).*

418 In order to make quantitative comparisons among the constant-relative density and -thickness
 419 specimens easier, the absorbed energy values of different specimens have been normalized by dividing
 420 them with the mass of the corresponding specimen (see [Figure 11](#) ~~Figure 11~~). It can be seen that the specific
 421 absorbed energy of all the plate-lattice specimens with constant relative density was higher than that for the
 422 constant thickness ones (except for BCC due to similar wall-thickness). In addition, in both the cases, hybrid
 423 specimens revealed a higher absorbed energy than the elementary ones. This was owing to the presence of
 424 the multiple sub-cells in the later and a simpler configuration in the former. The presence of larger number

425 of sub-cells delayed the premature-failure of the lattice structures by more effectual impact damage
 426 redistribution as reported in other investigations on various cellular structures [8, 47, 55, 56]. It can be
 427 evidently concluded that, the geometric hybridization in conjunction with the thickness distribution of each
 428 elementary structure in the hybrid plate-lattices transformed the brittle fracture into progressive damage of
 429 the plate-lattices.

430 3.3 Effect of relative density

431 *Figure 12* shows the typical energy-time and force-displacement plots of SC-BCC-FCC
 432 plate-lattices of various relative densities for an impact energy of 80 J. The results indicate that changing
 433 the relative density of the lattice structure considerably, will tune the impact response and damage
 434 mechanism. From the force-displacement curves (*Figure 12(b)*), it can be seen that ~~the~~ ~~the~~ ~~R55~~
 435 specimens with $\bar{\rho} = 55\%$ (see *Table 1*) exhibited the least maximum displacement and experience a
 436 steep initial slope (i.e. high initial stiffness). In addition, the initial stiffness and maximum displacement of
 437 the ~~R45~~-specimens $\bar{\rho} = 45\%$ approached nearly that of the ~~R55~~-specimens with $\bar{\rho} = 55\%$. This behavior
 438 indicates the brittle nature of the high relative density specimens. In contrast, the ~~R25~~-specimens with
 439 $\bar{\rho} = 25\%$ depicted the least stiffness and maximum displacement, indicating that it withstands the applied
 440 impact load in a ductile manner with higher strain-tolerance. Specimens fabricated with a $\bar{\rho} = 35\%$ relative
 441 density of 35% had an initial stiffness that lies between the abovementioned ones. Similar observations can
 442 be drawn in terms of the slope of the energy-time curves (*Figure 12(a)*). It is shown that the
 443 decrease in relative density of 3D plate-lattice structures will reduce the rigidity and will enable them to
 444 withstand the transient impact load in a ductile manner.



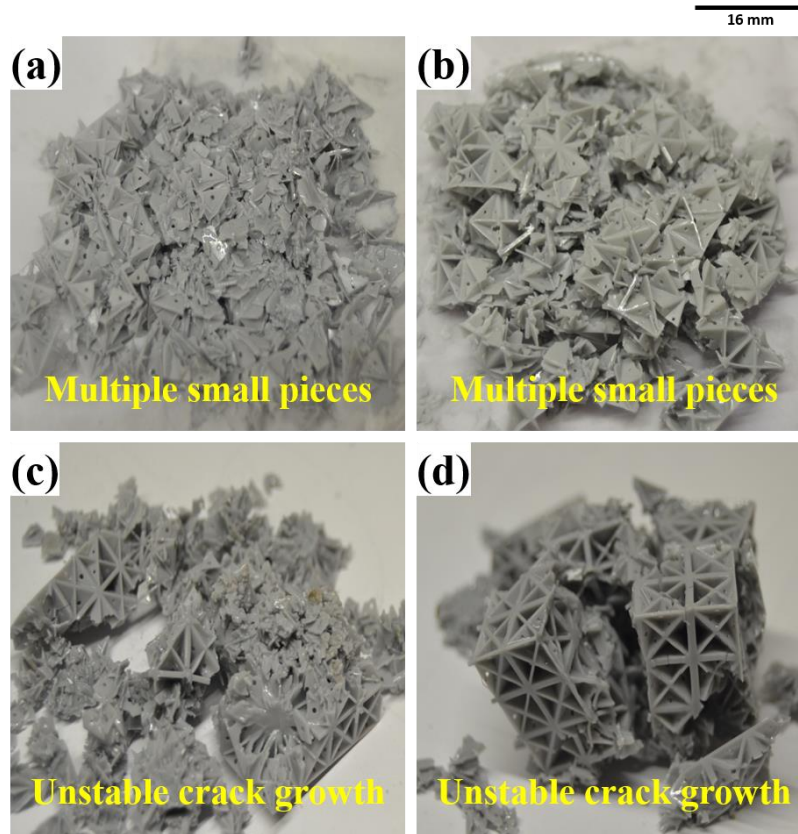
445
 446 *Figure 12*: Typical (a) energy vs. time and (b) contact force vs. displacement plots of SC-BCC-FCC lattice
 447 specimens for various relative densities under an impact energy of 80 J.

448 R55 specimens were the only structures ruptured at 54.26 J devoid of showing any sign of a short
449 plateau region in the energy-time curve (~~Figure 12~~~~Figure 12(a)~~) (the energy curve linearly increased with
450 time up until failure). A similar trace in the experimental curves had been noticed for the specimens
451 fabricated with a ~~$\bar{\rho}$ relative density of 45%~~. Nevertheless, there was a short plateau region and slight
452 oscillations at the trailing end of the energy-time and force displacement curves, respectively. On the other
453 hand, all the other specimens showed numerous distinct zones in the experimental curves as the impactor
454 crushed the specimens. For the ~~easespecimens with $\bar{\rho}=25%$ of R25 and $\bar{\rho}=35%$ R35 specimens~~, after the
455 initial peak, the load-displacement trace (~~Figure 12~~~~Figure 12(b)~~) oscillated for a long duration as the
456 impactor crushed through the specimens. However, the amplitude of the oscillation was higher in specimens
457 with a ~~$\bar{\rho}=35%$ relative density of 35%~~, suggesting a higher energy absorption behavior (*Figure S3*). The
458 ~~R35-specimens with $\bar{\rho}=35%$~~ showed a clear progressive increment in the energy-time history for a long
459 contact duration and multiple peaks in the contact force-displacement traces. The reasons for these
460 observations can be described by correlating the impact test results and the damage profile (~~Figure 13~~~~Figure~~
461 ~~13~~) of various specimens.

462 The debris of the plate-lattice specimens after the impact test were investigated to provide an in-
463 depth understanding of the damage mechanism. ~~Figure 13~~~~Figure 13~~ depicts the damage profile of the plate-
464 lattice specimens with various relative densities. The deformation profile is in direct correlation with the
465 relative density of the plate-lattice structure. It can be clearly seen in the figure that increasing the relative
466 density of the plate-lattice structures decreased the number of pieces smashed during the crushing process.
467 Plate-lattice specimens with a low relative density showed the most favorable deformation pattern through
468 smashing the specimens into multiple small pieces of debris or sub-cells (progressive local brittle failure)
469 [4]. On the contrary, high relative density specimens were smashed into finite number of pieces. Also, in
470 the case of high relative density specimens (specifically ~~$\bar{\rho}=55%$ R55~~), certain unit cells remained perfectly
471 intact even after the impact test.

472 The fracture of the high relative density specimens for an impactor maximum displacement of
473 around 5.6 mm (~~Figure 12~~~~Figure 12(b)~~) (~17.5% of the specimen's height) evidently indicates the
474 occurrence of unstable damage growth (brittle fracture). ~~In the case of~~~~For specimens with $\bar{\rho}=25%$ R25~~
475 ~~and $\bar{\rho}=35%$ R35-specimens~~ (low relative density), the presence of multiple small pieces of debris and the
476 high maximum displacement evidently indicates that most of the impact load was effectively redistributed
477 over different plates of the specimens. The moderate optimum with a relative density of 35% restricted
478 critical unstable crack growth unlike the stiff ~~R45 and R55-specimens~~ (~~$\bar{\rho}=45%$ and $\bar{\rho}=55%$~~), and further
479 provided a sufficient stiffness for the plate-lattices unlike the ~~R25-specimens~~ ~~with $\bar{\rho}=25%$~~ . These features,
480 as a result, improved the overall energy absorbing capability. From a comparison of the experimental curves

481 and damage profiles of various plate-lattice specimens as shown in [Figure 12](#) and [Figure](#)
482 [13](#) it can be concluded that the relative density significantly influenced the energy absorption
483 ability and the deformation pattern of the specimens.



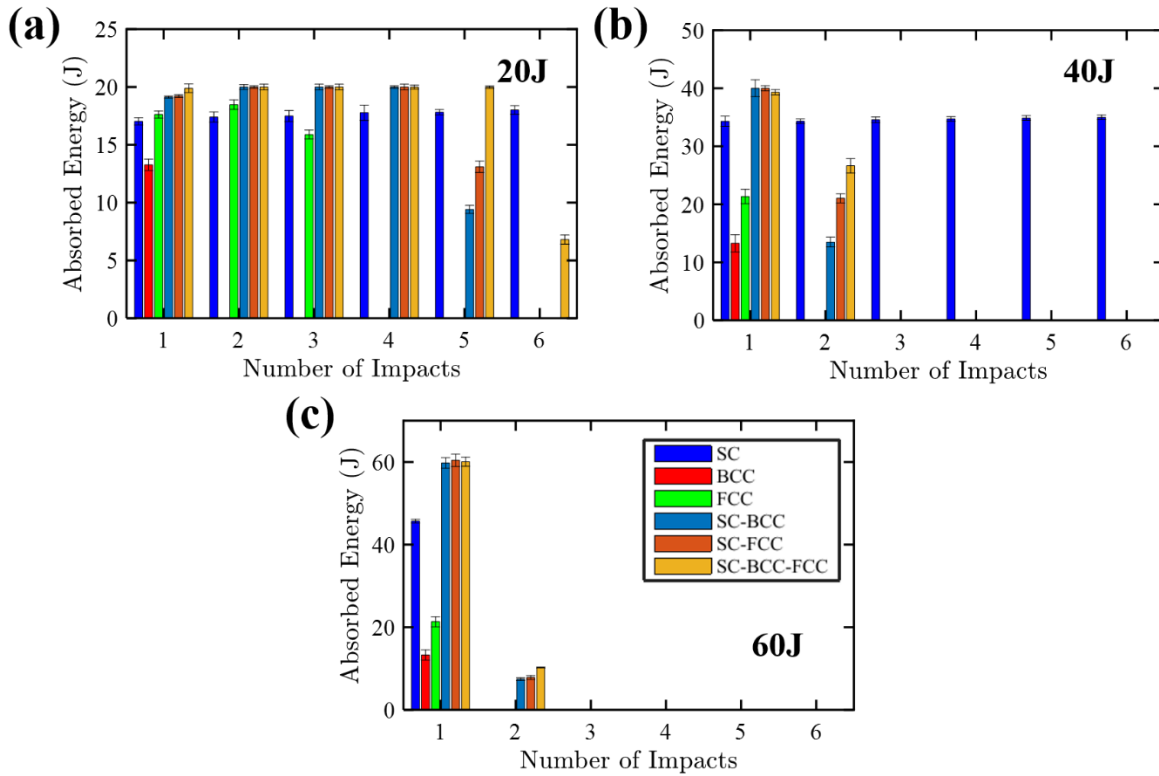
484
485 *Figure 13: Damage profile of SC-BCC-FCC specimens with various relative densities (a) $\bar{\rho} = 25\%$, (b)*
486 *$\bar{\rho} = 35\%$, (c) $\bar{\rho} = 45\%$ and (d) $\bar{\rho} = 55\%$ under impact energy of 80 J.*

487 **3.4 Effect of multiple impacts**

488 The sustained performance under repeated impacts is an important characteristic attribute of energy
489 absorbing structures [57]. In this study, six multiple low velocity impact tests were performed at impact
490 energy levels of 20, 40 and 60 J to examine the influence of multiple impacts on the energy absorbing
491 capabilities of various plate-lattice specimens and the corresponding results are shown in [Figure 14](#)
492 [14](#). The experimental results are shown up to the complete crushing of the specimens.

493 As expected, raising the impact energy level decreased the number of impacts to failure and caused
494 them to prematurely rupture. However, the number of impacts leading to complete failure of different plate-
495 lattice specimens were different and these values further changed with impact energy levels. In specific,
496 when the impact energy level was increased from 20 to 60 J, the number of impacts to failure changed from
497 6 to 1, 3 to 1, 5 to 2, 5 to 2 and 6 to 2 for SC, FCC, SC-BCC, SC-FCC and SC-BCC-FCC specimens,

498 respectively. The BCC specimens showed a complete rupture in the first impact (*Figure 14**Figure-14(a-c)*
 499 and *Figure S4*). Photographic images obtained from the impacted specimens (see *Figure S4, S5 and S6*)
 500 provided an insight into the damage mechanisms of different plate-lattice specimens under repeated impact
 501 loading. Obviously, there were several differences among the damage profiles of different specimens under
 502 multiple impacts at various impact energy levels.



503
 504 *Figure 14: Absorbed energy of various plate-lattice specimens subjected to multiple impacts at energy*
 505 *levels of (a) 20, (b) 40 and (c) 60 J.*

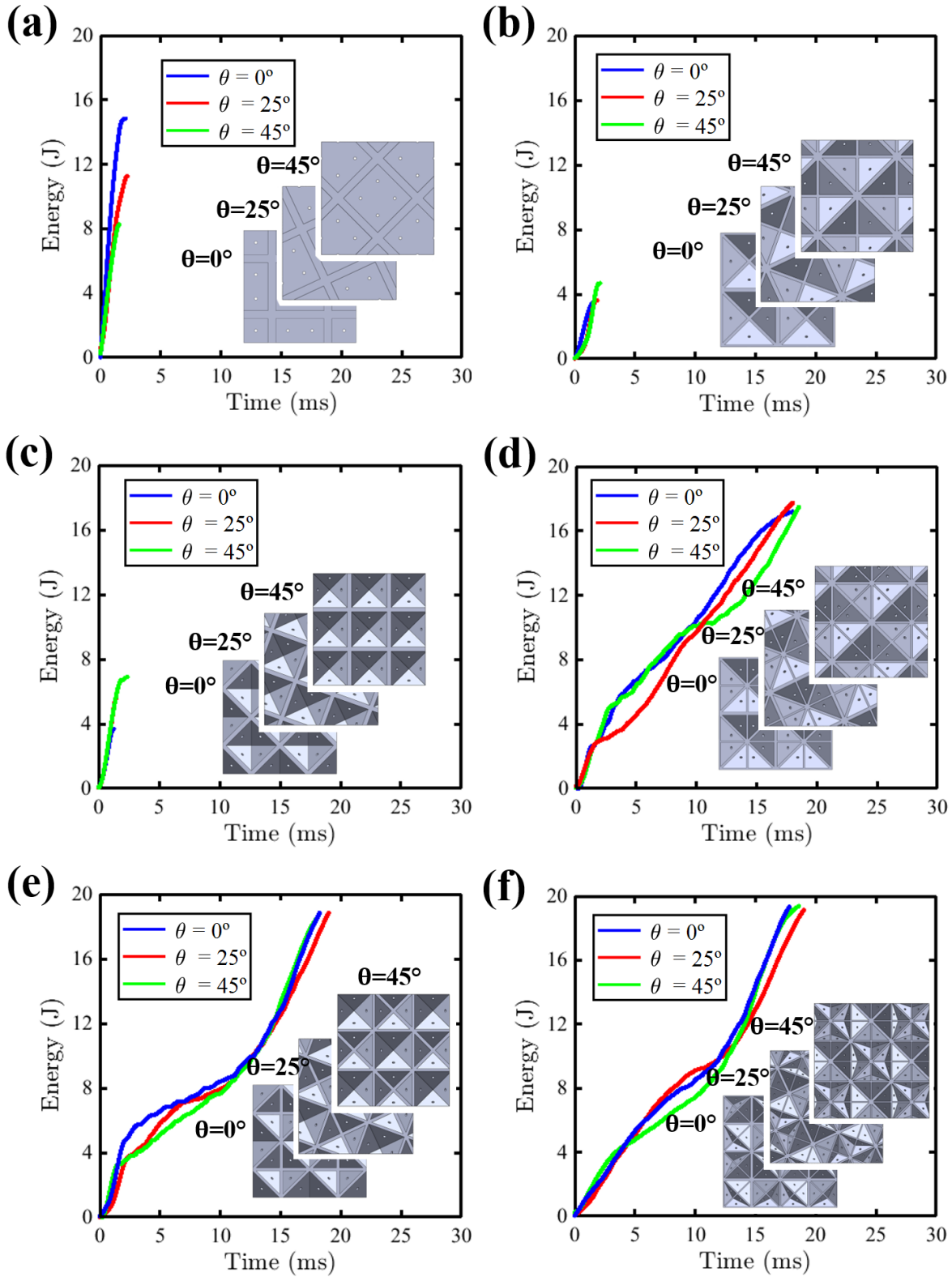
506 From *Figure 14**Figure-14(a)*, for an impact energy of 20 J, the SC specimens depicted the superior
 507 impact response. At this impact condition, there was some amount of elastic energy (i.e. rebound phase)
 508 remaining even after 6 multiple impacts. The lack of any visible permanent damage on the SC specimens
 509 in conjunction with absorption of a lower amount of impact energy during all the six impacts (see *Figure*
 510 *S4*) indicates the rebounding nature for all the six impacts [4]. This response obviously suggests that, for
 511 the damage onset, the number of impacts or the impact energy has to be raised further, highlighting its
 512 superior impact performance. It is well recognized that during the rebound phase the contact among
 513 impactor and specimen is lost significantly earlier prior to the impacted specimen returns to original position
 514 [58]. Considering that no visible damage was observed on the specimen during all the six impacts, the
 515 rebound phase was ascribed to high impact resistance of the specimen. The FCC specimens presented an

516 impact behavior more similar to SC specimens up to the second impact and abruptly failed in the subsequent
517 impact. At the same impact energy level, the impact behavior of all the hybrid specimens could be
518 characterized by “no elastic rebound” since the first impact owing to the presence of visible permanent
519 deformation. However, for the case of the hybrid specimens, the detected damage progressively increased
520 with the number of impacts, until the ultimate failure was reached. After being subjected to five impacts,
521 the SC-BCC and SC-FCC specimens absorbed about 9.41 J and 13.1 J of impact energy, respectively and
522 exhibited ultimate failure. The SC-BCC-FCC specimens depicted a better behavior with a more gradual
523 deformation pattern and failed in the sixth impact.

524 At an impact energy level of 40 J ([Figure 14](#)~~Figure-14~~(b)), the SC specimens endured the impact
525 load devoid of any permanent damage during the first impact and ruptured in the subsequent one (see *Figure*
526 *S5*). The FCC specimens failed prematurely during the first impact. Such premature failure can also be seen
527 in the hybrid specimens. However, at a higher impact energy level (60 J) ([Figure 14](#)~~Figure-14~~(c)), the
528 hybrid specimens depicted a higher number of impacts to ultimate failure than the elementary SC ones. The
529 SC specimens, despite presenting superior impact response when compared to the other specimens at 20
530 and 40 J, showed a poor impact resistance at 60 J (see *Figure S6*). The SC specimens exhibited ultimate
531 failure for a single impact. This phenomenon has been related to the energy dissipation mechanism of SC
532 specimens through catastrophic brittle fracture whereas all the hybrid specimens progressively dissipated
533 the impact energy and failed in the second impact, as confirmed by the photographic images of the damaged
534 specimens. It was apparent that, due to large number of sub-cells distributing the impact load at higher
535 impact energy levels, hybrid specimens were outperforming elementary ones.

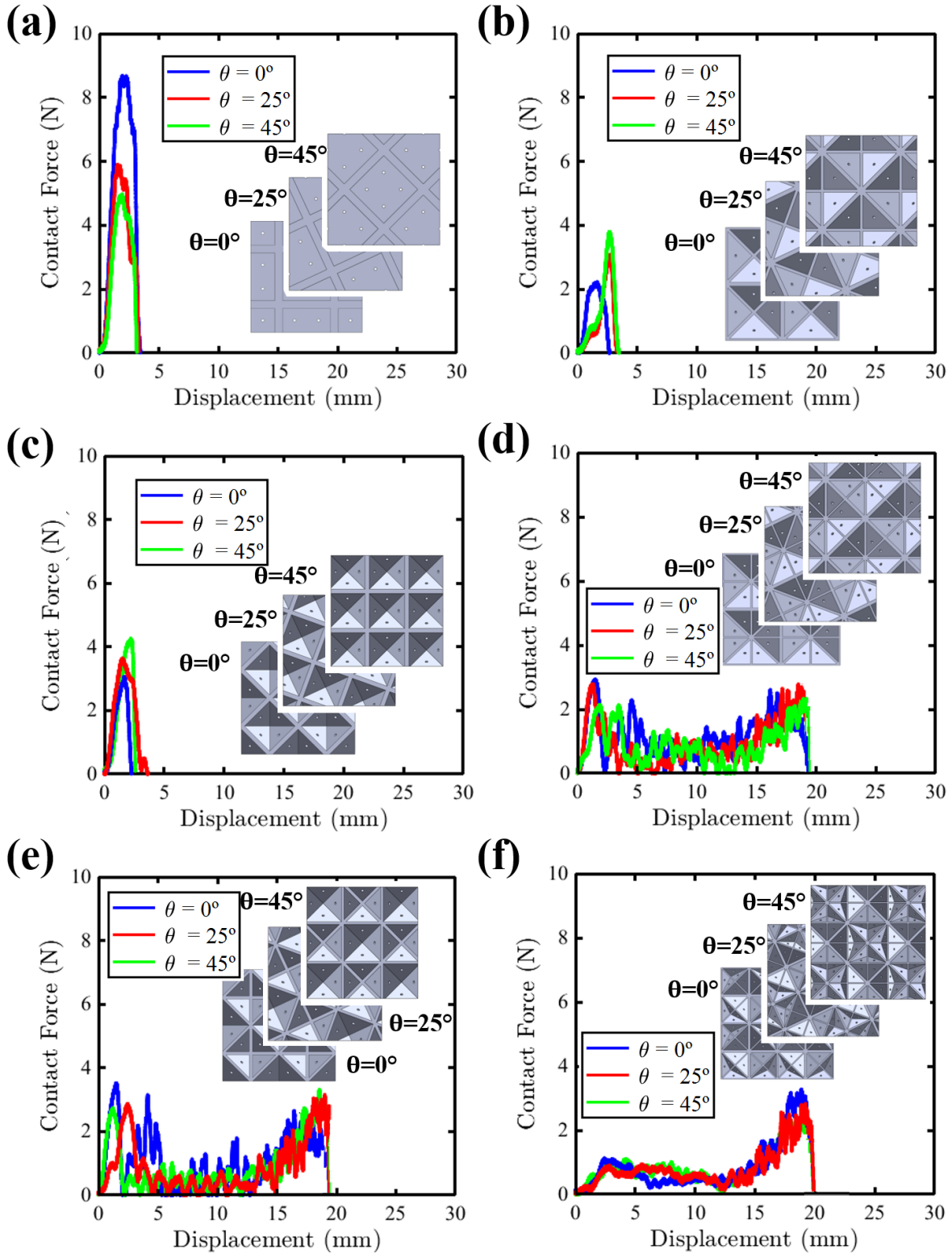
536 **3.5 Effect of impact angle**

537 As a matter of fact, most of the impact events in real-time scenario occur in an oblique manner
538 [42]. It is an important concern on the way, to study, while configuring the energy absorbing cellular
539 structures so that structures are capable of enduring both transverse and oblique impact loads. Energy-time
540 and contact force-displacement curves of various plate-lattice specimens for every tested angle (0°, 25° and
541 45°), are presented in [Figure 15](#)~~Figure-15~~ and [Figure 16](#)~~Figure-16~~, respectively at an impact energy of 20
542 J. The peak contact-force and absorbed energy of the elementary specimens changed with the angle of
543 impact. Moreover, for all the impact angles, the elementary specimens exhibited a brittle response, failing
544 by a single, and sudden, load drop after reaching the peak contact force. For the SC specimens, the absorbed
545 energy clearly reduced with increasing angle of impact from 0° to 45°; on the contrary, the BCC and FCC
546 specimens showed an increasing trend ([Figure 15](#)~~Figure-15~~(a-c)). For SC specimens, the absorbed energy
547 along the diagonal directions (45°) was significantly lower than at 0° [12].



548

549 *Figure 15: Energy-time curves of various plate-lattice specimens (a) SC, (b) BCC, (c) FCC, (d) SC-BCC,*
 550 *(e) SC-FCC and (f) SC-BCC-FCC for 0° , 25° and 45° tested angles ($\bar{\rho} = 35\%$)*



551

552 *Figure 16: Contact force-displacement curves various plate-lattice specimens (a) SC, (b) BCC, (c) FCC,*
 553 *(d) SC-BCC, (e) SC-FCC and (f) SC-BCC-FCC tested at 0°, 25° and 45° angles ($\bar{\rho} = 35\%$).*

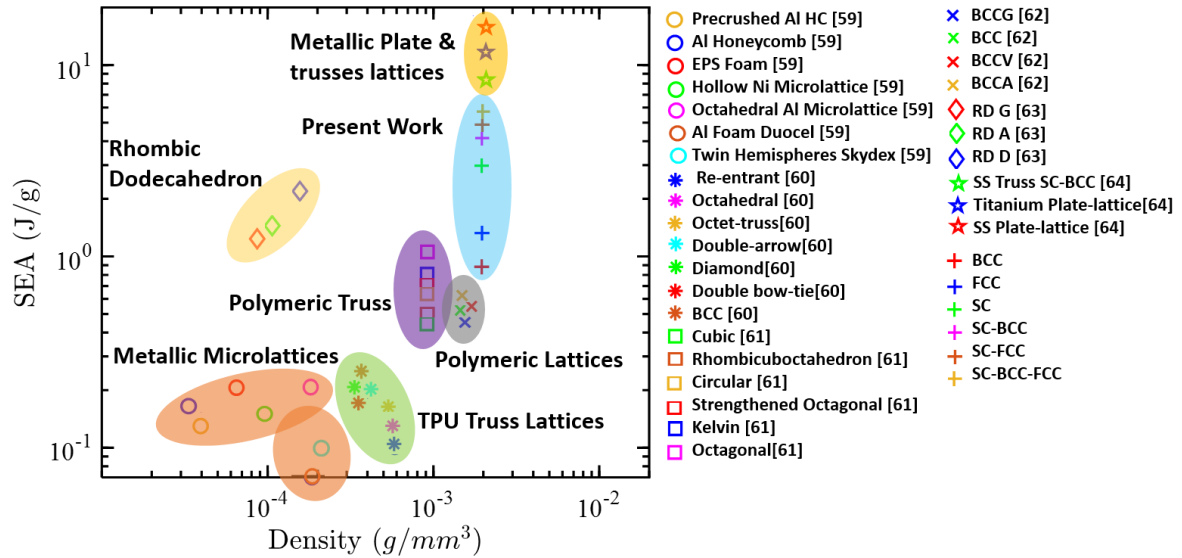
554 The energy-time histories of every hybrid specimen depicted almost the same trend for all the tested
555 angles ([Figure 15](#)~~Figure 15(d-f)~~), and further, the loading and unloading part of the load-displacement
556 curves were nearly identical ([Figure 15](#)~~Figure 16(d-f)~~); in specific, identical smooth and oscillation patterns
557 were observed during the loading and unloading phase, respectively, suggesting that the damage
558 progression for all the impact angles were identical.

559 For all the hybrid specimens, the absorbed energies at 0° , 25° and 45° were almost the same, and
560 the maximum difference in the absorbed energies was around 2.9% ([Figure S7](#)), which is much lower than
561 the experimental scatter observed for every elementary specimen at various impact angles (30.13% lowest
562 for BCC). The unloading part of contact force-displacement curves in all the specimens (including the
563 elementary ones) was almost coincident ([Figure 16](#)~~Figure 16(a-f)~~). Consequently, the maximum
564 displacement was independent of the impact angle, as reported elsewhere [42]. Similar to the maximum
565 displacement, the contact duration varied considerably with the plate-lattice configuration. However, the
566 differences among different impact angles were within the experimental scatter; therefore, the contact
567 duration is another independent parameter of the angle of impact.

568 For all the impact angles, the plate-lattice specimens can be ranked from the higher to the lower
569 absorbed energy in the following order: SC-BCC-FCC > SC-FCC > SC-BCC > FCC > BCC > SC ([Figure](#)
570 [S7](#)). It can be observed that the absorbed energy of SC-BCC-FCC specimens was higher than that of the
571 other plate-lattice specimens. This behavior was noticed for all the impact angles considered in this work.
572 The trend in the variation of peak contact force coincides well with the observations made for the absorbed
573 energy of various specimens ([Figure 16](#)~~Figure 16~~). The hybrid specimens achieve a direction-independent
574 impact response through multiple repeating structures of open or closed cells in all the directions. Hybrid
575 structures were found to have a directional independent behavior assuming linear elasticity as reported in
576 [38]. In this study, we observed that energy-time and load-deformation traces followed almost similar
577 behavior independent of the angle of impact up to failure.

578 **3.6. Comparative energy absorption characteristics of SC-BCC-FCC hybrid 3D-plate lattices**

579 The SC-BCC-FCC specimens exhibit a specific energy absorption (SEA) capacity of 5.07 J/g,
580 which is comparable to that of the titanium and stainless-steel lattice structures. Moreover, the SEA capacity
581 of SC-BCC-FCC lattices is higher than that of the conventional aluminum lattices and other metamaterials,
582 as depicted [Figure 17](#)~~Figure 17~~. Comparatively, the lightweight titanium alloy foams show outstanding
583 energy absorption performance. However, fabrication of these structures via processes such as EBM, laser
584 cladding, etc. is expensive and energy consuming as compared with SLA additive manufacturing approach
585 used in this study for the fabrication of lightweight polymeric lattices.



586

587 Figure 17: Comparison of specific energy absorption of the plate-lattices considered in the present work
 588 with the extant literature.

589 **4. Conclusions**

590 In this paper, different elementary (SC, BCC and FCC) and hybrid (SC-BCC, SC-FCC and SC-
 591 BCC-FCC) 3D plate-lattice structures were designed and 3D printed using the stereolithography (SLA)
 592 additive manufacturing technique. The dynamic crushing behavior and energy absorption characteristics of
 593 different plate-lattice structures were investigated through low-velocity drop weight impact tests. The
 594 effects of the impact energy, relative density, plate-thickness, repetitive impacts and impact angle on the
 595 dynamic impact behavior of various plate-lattice structures were investigated. The following important
 596 conclusions can be drawn from the experimental test results:

- 597 1. The plate-lattice configuration heavily influenced the dynamic impact behavior, with hybrid
 598 structures outperforming elementary ones, progressively as the impact energy raises. The SC-BCC-
 599 FCC specimens exhibited the highest toughness, followed by the SC-FCC, SC-BCC, SC, FCC and
 600 BCC specimens.
- 601 2. The hybrid lattice structures, due to the presence of large number of open and closed sub-cells,
 602 were able to attenuate the peak impact stress transmitted to the structure and extend the duration of
 603 the load pulse (high toughness). Moreover, at all impact energy levels, the energy-time history
 604 progressively increased, until the maximum energy was absorbed, exhibiting a progressive failure
 605 behavior.
- 606 3. Irrespective of the relative density, the thickness distribution of every elementary structure in the
 607 plate-lattices played an important role in mitigating the deleterious brittle fracture, promoting
 608 progressive damage. This has led to enhanced energy absorption characteristics.

- 609 4. ~~The moderate~~The moderate optimum relative density ($\bar{\rho}=35\%$) ~~of 35% specimens~~ restricted
610 critical unstable crack growth unlike the stiff ~~R45 and R55~~ specimens ($\bar{\rho}=45\%$ and $\bar{\rho}=55\%$), and
611 further provided a sufficient stiffness for the plate-lattices unlike the ~~R25~~ specimens with $\bar{\rho}=25\%$.
612 These features, as a result, improved the overall energy absorbing capability.
- 613 5. The multiple-impact response of various plate lattice specimens varied considerably with the
614 increase in impact energy. When the impact energy was increased from 20 to 60 J, the number of
615 impacts to failure changed from 6 to 1, 3 to 1, 5 to 2, 5 to 2 and 6 to 2 for SC, FCC, SC-BCC, SC-
616 FCC and SC-BCC-FCC specimens, respectively. The BCC specimens showed a complete rupture
617 in the first impact.
- 618 6. The hybrid specimens showed a direction-independent impact response. The absorbed energy at
619 impact angles of 0° , 25° and 45° were almost coinciding, and the maximum difference in the
620 absorbed energy was about 2.90%, which is much lower than the experimental scatter observed for
621 every elementary specimen at various impact angles.
- 622 7. The SC-BCC-FCC lattices exhibit higher specific energy absorption than that of the conventional
623 aluminum lattices and other practical metamaterials.

624 Acknowledgements

625
626 Authors would like to thank to Abu Dhabi National Oil Company (ADNOC) for providing the research
627 grant (Award No: EX2016-000010). SK would like to thank the University of Glasgow for the start-up
628 grant.

629 References:

- 630
631 1. Al-Saedi, D.S.J., et al., *Mechanical properties and energy absorption capability of functionally*
632 *graded F2BCC lattice fabricated by SLM*. Materials & Design, 2018. **144**: p. 32-44.
- 633 2. Wang, Z. and J. Liu, *Mechanical performance of honeycomb filled with circular CFRP tubes*.
634 Composites Part B: Engineering, 2018. **135**: p. 232-241.
- 635 3. Ashby, M., *The properties of foams and lattices*. Philosophical Transactions of the Royal Society
636 A: Mathematical, Physical and Engineering Sciences, 2005. **364**(1838): p. 15-30.
- 637 4. Andrew, J.J., et al., *Impact performance enhancement of honeycombs through additive*
638 *manufacturing-enabled geometrical tailoring*. International Journal of Impact Engineering, 2019.
639 **134**: p. 103360.
- 640 5. Habib, F.N., et al., *Fabrication of polymeric lattice structures for optimum energy absorption*
641 *using Multi Jet Fusion technology*. Materials & Design, 2018. **155**: p. 86-98.
- 642 6. Zheng, X., et al., *Ultralight, ultrastiff mechanical metamaterials*. Science, 2014. **344**(6190): p.
643 1373-1377.
- 644 7. Xiao, L. and W. Song, *Additively-manufactured functionally graded Ti-6Al-4V lattice structures*
645 *with high strength under static and dynamic loading: Experiments*. International Journal of
646 Impact Engineering, 2018. **111**: p. 255-272.

- 647 8. Gibson, L.J. and M.F. Ashby, *Cellular Solids: Structure and Properties*. 2 ed. Cambridge Solid State
648 Science Series. 1997, Cambridge: Cambridge University Press.
- 649 9. Duoss, E.B., et al., *Three-dimensional printing of elastomeric, cellular architectures with negative*
650 *stiffness*. *Advanced Functional Materials*, 2014. **24**(31): p. 4905-4913.
- 651 10. Srivastava, V. and R. Srivastava, *On the polymeric foams: modeling and properties*. *Journal of*
652 *materials science*, 2014. **49**(7): p. 2681-2692.
- 653 11. Grenestedt, J., *On interactions between imperfections in cellular solids*. *Journal of materials*
654 *science*, 2005. **40**(22): p. 5853-5857.
- 655 12. Tancogne-Dejean, T., et al., *3D Plate-Lattices: An Emerging Class of Low-Density Metamaterial*
656 *Exhibiting Optimal Isotropic Stiffness*. *Advanced Materials*, 2018. **30**(45): p. 1803334.
- 657 13. Helou, M. and S. Kara, *Design, analysis and manufacturing of lattice structures: an overview*.
658 *International Journal of Computer Integrated Manufacturing*, 2018. **31**(3): p. 243-261.
- 659 14. Savio, G., R. Meneghello, and G. Concheri, *Geometric modeling of lattice structures for additive*
660 *manufacturing*. *Rapid Prototyping Journal*, 2018. **24**(2): p. 351-360.
- 661 15. Klahn, C., B. Leutenecker, and M. Meboldt, *Design Strategies for the Process of Additive*
662 *Manufacturing*. *Procedia CIRP*, 2015. **36**: p. 230-235.
- 663 16. Bourell, D.L., *Perspectives on Additive Manufacturing*. *Annual Review of Materials Research*,
664 2016. **46**(1): p. 1-18.
- 665 17. Kumar, S., et al., *Tunable Energy Absorption Characteristics of Architected Honeycombs Enabled*
666 *via Additive Manufacturing*. *ACS Applied Materials & Interfaces*, 2019. **11**(45): p. 42549-42560.
- 667 18. Quinlan, H.E., et al., *Industrial and Consumer Uses of Additive Manufacturing: A Discussion of*
668 *Capabilities, Trajectories, and Challenges*. *Journal of Industrial Ecology*, 2017. **21**(S1): p. S15-S20.
- 669 19. Zheng, X., et al., *Ultralight, ultrastiff mechanical metamaterials*. *Science*, 2014. **344**(6190): p.
670 1373-1377.
- 671 20. Duoss, E.B., et al., *Three-Dimensional Printing of Elastomeric, Cellular Architectures with*
672 *Negative Stiffness*. *Advanced Functional Materials*, 2014. **24**(31): p. 4905-4913.
- 673 21. Tancogne-Dejean, T. and D. Mohr, *Elastically-isotropic truss lattice materials of reduced plastic*
674 *anisotropy*. *International Journal of Solids and Structures*, 2018. **138**: p. 24-39.
- 675 22. Ling, C., et al., *Mechanical behaviour of additively-manufactured polymeric octet-truss lattice*
676 *structures under quasi-static and dynamic compressive loading*. *Materials & Design*, 2019. **162**:
677 p. 106-118.
- 678 23. Tancogne-Dejean, T., A.B. Spierings, and D. Mohr, *Additively-manufactured metallic micro-lattice*
679 *materials for high specific energy absorption under static and dynamic loading*. *Acta Materialia*,
680 2016. **116**: p. 14-28.
- 681 24. Mohr, D., *Mechanism-based multi-surface plasticity model for ideal truss lattice materials*.
682 *International Journal of Solids and Structures*, 2005. **42**(11): p. 3235-3260.
- 683 25. Gümrük, R. and R.A.W. Mines, *Compressive behaviour of stainless steel micro-lattice structures*.
684 *International Journal of Mechanical Sciences*, 2013. **68**: p. 125-139.
- 685 26. Gümrük, R., R.A.W. Mines, and S. Karadeniz, *Static mechanical behaviours of stainless steel*
686 *micro-lattice structures under different loading conditions*. *Materials Science and Engineering: A*,
687 2013. **586**: p. 392-406.
- 688 27. Harris, J.A., R.E. Winter, and G.J. McShane, *Impact response of additively manufactured metallic*
689 *hybrid lattice materials*. *International Journal of Impact Engineering*, 2017. **104**: p. 177-191.
- 690 28. Mines, R., et al., *Drop weight impact behaviour of sandwich panels with metallic micro lattice*
691 *cores*. *International Journal of Impact Engineering*, 2013. **60**: p. 120-132.
- 692 29. Meza, L.R., S. Das, and J.R. Greer, *Strong, lightweight, and recoverable three-dimensional*
693 *ceramic nanolattices*. *Science*, 2014. **345**(6202): p. 1322-1326.

- 694 30. Ahmadi, S., et al., *Additively manufactured open-cell porous biomaterials made from six different*
695 *space-filling unit cells: The mechanical and morphological properties*. *Materials*, 2015. **8**(4): p.
696 1871-1896.
- 697 31. Jin, N., et al., *Failure and energy absorption characteristics of four lattice structures under*
698 *dynamic loading*. *Materials & Design*, 2019. **169**: p. 107655.
- 699 32. Thomas, M. and J.-R. Alluru, *Thriving in a downturn: aligning corporate strategy and the*
700 *economic context to ensure stable growth*. *Strategic Direction*, 2016. **32**(2): p. 14-16.
- 701 33. Gurtner, G. and M. Durand, *Stiffest elastic networks*. *Proceedings of the Royal Society A:*
702 *Mathematical, Physical and Engineering Sciences*, 2014. **470**(2164): p. 20130611.
- 703 34. Hashin, Z. and S. Shtrikman, *A variational approach to the theory of the elastic behaviour of*
704 *multiphase materials*. *Journal of the Mechanics and Physics of Solids*, 1963. **11**(2): p. 127-140.
- 705 35. Berger, J., H. Wadley, and R. McMeeking, *Mechanical metamaterials at the theoretical limit of*
706 *isotropic elastic stiffness*. *Nature*, 2017. **543**(7646): p. 533.
- 707 36. Han, S.C., J.W. Lee, and K. Kang, *A new type of low density material: Shellular*. *Advanced*
708 *Materials*, 2015. **27**(37): p. 5506-5511.
- 709 37. Ozdemir, Z., et al., *Energy absorption in lattice structures in dynamics: Nonlinear FE simulations*.
710 *International Journal of Impact Engineering*, 2017. **102**: p. 1-15.
- 711 38. Lee, S., et al., *Dynamic failure of metallic pyramidal truss core materials – Experiments and*
712 *modeling*. *International Journal of Plasticity*, 2006. **22**(11): p. 2118-2145.
- 713 39. Liu, Y.D., et al., *A numerical study on the rate sensitivity of cellular metals*. *International Journal*
714 *of Solids and Structures*, 2009. **46**(22): p. 3988-3998.
- 715 40. Qiao, J. and C.Q. Chen, *Analyses on the In-Plane Impact Resistance of Auxetic Double Arrowhead*
716 *Honeycombs*. *Journal of Applied Mechanics*, 2015. **82**(5): p. 051007-051007-9.
- 717 41. Hou, S., et al., *Mechanical properties of sandwich composites with 3d-printed auxetic and non-*
718 *auxetic lattice cores under low velocity impact*. *Materials & Design*, 2018. **160**: p. 1305-1321.
- 719 42. Ivañez, I., et al., *The oblique impact response of composite sandwich plates*. *Composite*
720 *Structures*, 2015. **133**: p. 1127-1136.
- 721 43. Navarro, P., et al., *Experimental and numerical study of oblique impact on woven composite*
722 *sandwich structure: Influence of the firing axis orientation*. *Composite Structures*, 2012. **94**(6): p.
723 1967-1972.
- 724 44. Deshpande, V., M. Ashby, and N. Fleck, *Foam topology: bending versus stretching dominated*
725 *architectures*. *Acta materialia*, 2001. **49**(6): p. 1035-1040.
- 726 45. Bouville, F., et al., *Strong, tough and stiff bioinspired ceramics from brittle constituents*. *Nature*
727 *materials*, 2014. **13**(5): p. 508.
- 728 46. Wegst, U.G., et al., *Bioinspired structural materials*. *Nature materials*, 2015. **14**(1): p. 23.
- 729 47. Zhou, J., et al., *The low velocity impact response of foam-based sandwich panels*. *Composites*
730 *Science and Technology*, 2012. **72**(14): p. 1781-1790.
- 731 48. Sarasini, F., et al., *Drop-weight impact behaviour of woven hybrid basalt–carbon/epoxy*
732 *composites*. *Composites Part B: Engineering*, 2014. **59**: p. 204-220.
- 733 49. Andrew, J.J., S.M. Srinivasan, and A. Arockiarajan, *The role of adhesively bonded super hybrid*
734 *external patches on the impact and post-impact response of repaired glass/epoxy composite*
735 *laminates*. *Composite Structures*, 2018. **184**: p. 848-859.
- 736 50. Andrew, J.J., et al., *Parameters influencing the impact response of fiber-reinforced polymer*
737 *matrix composite materials: A critical review*. *Composite Structures*, 2019. **224**: p. 111007.
- 738 51. Andrew, J.J., S.M. Srinivasan, and A. Arockiarajan, *Influence of patch lay-up configuration and*
739 *hybridization on low velocity impact and post-impact tensile response of repaired glass fiber*
740 *reinforced plastic composites*. *Journal of Composite Materials*, 2019. **53**(1): p. 3-17.

- 741 52. Zhang, Y., et al., *Static and dynamic crushing responses of CFRP sandwich panels filled with*
742 *different reinforced materials*. *Materials & Design*, 2017. **117**: p. 396-408.
- 743 53. Wang, T., et al., *Mechanical Response of Square Honeycomb Sandwich Plate with Asymmetric*
744 *Face Sheet Subjected to Blast Loading*. *Procedia Engineering*, 2011. **23**: p. 457-463.
- 745 54. A Jansen, J. and S. Technimet, *FRACTOGRAPHIC CHARACTERIZATION OF POLYCARBONATE*
746 *FAILURE MODES*. 2019.
- 747 55. Dharmasena, K., et al., *Mechanical Response of Metallic Honeycomb Sandwich Panel Structures*
748 *to High-Intensity Dynamic Loading*. Vol. 35. 2008. 1063-1074.
- 749 56. Hasan, R., et al., *Comparison of the Drop Weight Impact Performance of Sandwich Panels with*
750 *Aluminium Honeycomb and Titanium Alloy Micro Lattice Cores*. *Applied Mechanics and*
751 *Materials*, 2010. **24-25**: p. 413-418.
- 752 57. Jefferson Andrew, J., et al., *Compression after impact strength of repaired GFRP composite*
753 *laminates under repeated impact loading*. *Composite Structures*, 2015. **133**: p. 911-920.
- 754 58. Minak, G., et al., *EQUIVALENT STIFFNESS AS MEASURE OF LOW VELOCITY IMPACT DAMAGE OF*
755 *COMPLEX COMPOSITE STRUCTURES* [22]. Vol. Vol.10. 2012. 91-104.
- 756 59. Schaedler, Tobias A., Christopher J. Ro, Adam E. Sorensen, Zak Eckel, Sophia S. Yang, William B.
757 Carter, and Alan J. Jacobsen. "Designing metallic microlattices for energy absorber applications."
758 *Advanced Engineering Materials* 16, no. 3 (2014): 276-283.
- 759 60. Wu, Y., J. Hermes, L. Verbelen, and L. Yang. "Impact energy absorption ability of thermoplastic
760 polyurethane (TPU) cellular structures fabricated via powder bed fusion."
- 761 61. Habib, F. N., P. Iovenitti, S. H. Masood, and M. Nikzad. "Fabrication of polymeric lattice structures
762 for optimum energy absorption using Multi Jet Fusion technology." *Materials & Design* 155
763 (2018): 86-98.
- 764 62. Al Rifaie, Mohammed Jamal. "Resilience and Toughness Behavior of 3D-Printed Polymer Lattice
765 Structures: Testing and Modeling." PhD diss., Wright State University, 2017.
- 766 63. Cao, Xiaofei, Dengbao Xiao, Ying Li, Weibin Wen, Tian Zhao, Zihao Chen, Yongbo Jiang, and Daining
767 Fang. "Dynamic compressive behavior of a modified additively manufactured rhombic
768 dodecahedron 316L stainless steel lattice structure." *Thin-Walled Structures* 148 (2020): 106586.
- 769 64. Tancogne-Dejean, T., X. Li, M. Diamantopoulou, C. C. Roth, and D. Mohr. "High strain rate
770 response of additively-manufactured plate-lattices: experiments and modeling." *Journal of*
771 *Dynamic Behavior of Materials* 5, no. 3 (2019): 361-375.